Petroleum Science 23 (2026) 33–51

Contents lists available at ScienceDirect

Petroleum Science

journal homepage: www.keaipublishing.com/en/journals/petroleum-science

Original Paper

Multiscale anisotropic mechanical properties of oil shale: New insights from nanoindentation profiling

Zi-Geng Pei [a,b], Guang-Lei Cui [a,b,*], Yong-Ting Duan [a,b], Yu-Ling Tan [c], Derek Elsworth [d], Wang-Xing Cheng [e], Ning-Liang Sun [f], Zhe-Jun Pan [g]

[a] State Key Laboratory of Intelligent Deep Metal Mining and Equipment, Northeastern University, Shenyang, 110819, Liaoning, China
[b] Key Laboratory of Liaoning Province On Deep Engineering nd Intelligent Technology, Northeastern University, Shenyang, 110819, Liaoning, China
[c] Department of Engineering Mechanics, Shijiazhuang Tiedao University, Shijiazhuang, 050043, Hebei, China
[d] Energy and Mineral Engineering, G3 Center and Energy Institute, Pennsylvania State University, University Park, PA, 16802, USA
[e] Department of Geotechnical Engineering, College of Civil Engineering, Tongji University, Shanghai, 200092, China
[f] Institute of Ocean Engineering, Northeastern University at Qinhuangdao, Qinhuangdao, 066004, Hebei, China
[g] State Key Laboratory of Continental Shale Oil, Northeast Petroleum University, Daqing, 163318, Heilongjiang, China

ARTICLE INFO

Article history:
Received 19 February 2025
Received in revised form
10 June 2025
Accepted 8 September 2025
Available online 10 September 2025

Edited by Xi Zhang and Jie Hao

Keywords:
Lacustrine shale
Multiscale anisotropy
Clustering method
Upscaling method
Homogenization analysis

ABSTRACT

Oil shale reservoirs are characterized by significant heterogeneity in mineral components and pronounced anisotropy in micromechanical properties—both influencing resource recovery. We couple fine-scale nanoindentation and mineral analyzer (Tescan Integrated Mineral Analyzer (TIMA)) profiling of the mechanical properties and components of oil shale samples from the Ordos Basin, China. We use an updated clustering method, including a more precise way to delineate mineral boundaries, to precisely categorize the numerous nanoindentation test data into mineral composition groups. The lowest-to-highest ranking of Young's modulus and fracture toughness values in our samples is in the order clay, quartz, feldspar, dolomite, and then pyrite. Anisotropic characteristics of each phase were determined at various scales, with values of Young's modulus and fracture toughness are higher on surfaces parallel to the bedding plane than on those perpendicular to it. The clay-rich dark phase exhibits lower Young's modulus, making its pore structures more prone to collapse during gas depletion. Conversely, the fracture toughness of the bright phase is higher than that of the dark phase, causing the hydraulic fracturing to more easily penetrate through the dark phase and stop at the bright phase boundary. These divergences in mechanical properties are caused by the microstructure of the oil shale during sedimentation: the discrete distribution of hard minerals in the bright phase constrains deformation, while the lamellar clay layers in the dark phase provide less restriction. Upgraded mesoscopic mechanical parameters obtained from the modified Mori-Tanaka method, incorporating a shape factor, return results close to reality. Young's modulus and fracture toughness are lower at the mesoscale than at the microscale, indicating greater rigidity and toughness in fine structures. This study provides important insights into the cross-scale deformation and fracture behavior of shale, highlighting its impact on reservoir deformation, fracture propagation, and oil recovery efficiency.

1. Introduction

Lacustrine oil shale reservoirs (Fig. 1(a)) are recognized as a significant alternative resource because of their substantial contribution to world energy (Duan et al., 2024; Fu et al., 2020; Guo et al., 2024). Such reservoirs present significant heterogeneity in mineral composition, comprising multiple mineral components often observed in bright and dark phases at mesoscale (~ cm scale). Recent nanoindentation results on the caprock formation in

* Corresponding author.
E-mail address: cuiguanglei@mail.neu.edu.cn (G.-L. Cui).
Peer review under the responsibility of China University of Petroleum (Beijing).

https://doi.org/10.1016/j.petsci.2025.09.011

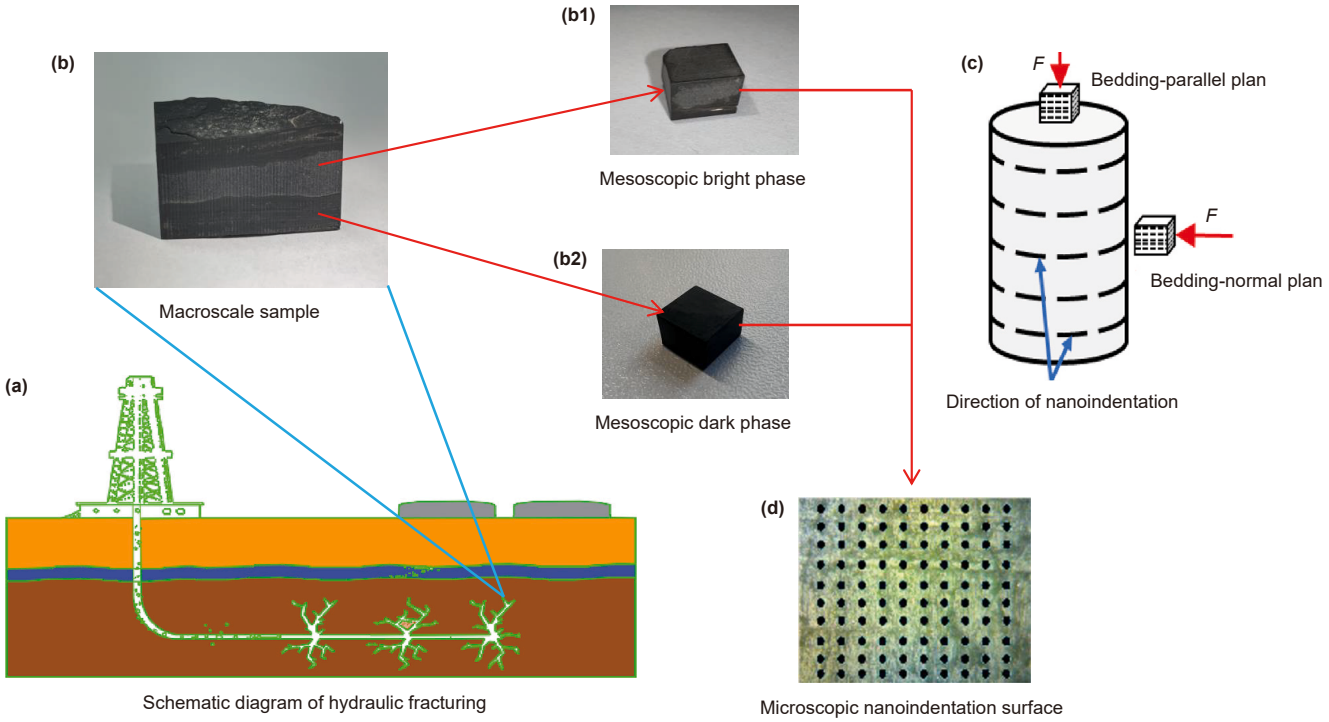

Fig. 1. Multiscale schematic of reservoir. **(a)** Hydraulic fracturing at field scale. **(b)** Mesoscale sample of Ordos lacustrine shale. Sub-sample of Ordos lacustrine laminated shale, for **(b1)** bright and **(b2)** dark phase samples. **(c)** Schematic of loading direction for nanoindentation as bedding-normal and bedding-parallel (accessing the bedding face) and **(d)** Mmicroscale nano indented shale sample surface.

Daqing reveal notable elastic anisotropy across all major mineral constituents, with anisotropy ratios ranging from 1.01 to 1.96 depending on mineral type and orientation (Wu et al., 2020). Despite extensive studies on the geological attributes of lacustrine shale, little attention has been devoted to understanding the variations in mechanical properties across different minerals, orientations, phases and scales (Chalmers et al., 2012; Loucks et al., 2009; Vernik and Milovac, 2011). These limitations hinder the efficient exploitation of oil shale reservoirs and highlight the necessity of investigating the anisotropy and characteristics of each phase from microscale to mesoscale.

Lacustrine shales are broadly classified into massive and laminated shales (Li et al., 2017; Liang et al., 2018; S. Wang et al., 2021). The latter term, associated with higher oil content, is generally identified by alternating bright and dark phases (Fig. 1(b) (Liao et al., 2024; Wang et al., 2014; Yuan et al., 2015)). The mineral percentage and mechanical properties display significant differences within these two phases (Bohacs et al., 2000; Hu et al., 2022; Zhao et al., 2019). The bright phase predominantly consists of hard minerals (e.g. quartz) and the dark phase predominantly clay minerals (e.g. illite and montmorillonite) (Hupp and Donovan, 2018). As a result, the bright phase has a higher mechanical strength and a lower compressibility at the sample scale (Zhang et al., 2021) and the dark phase the converse with a higher propensity for plastic deformation or creep (Zhu et al., 2019). In addition, the laminated structure significantly influences the mechanical properties along bedding and perpendicular that bedding (Sone and Zoback, 2013). Generally, the mechanical properties, such as stiffness and strength, are lower in the direction perpendicular to the laminae (bedding faces) compared to those in the parallel direction (Hu et al., 2024; Tan et al., 2014). In summary, the mineralogical and structural differences between bright and dark phases, along with the laminated structure, significantly influence the mechanical properties and anisotropy of lacustrine shales.

The micromechanical properties of minerals within oil shales, such as Young's modulus and fracture toughness, play a crucial role in determining the mechanical behavior at both meso- and macro-scales (Cheng et al., 2025a; Evans, 1990). Nanoindentation, a non-destructive instrumental indentation technique (Schuh, 2006), has been used to investigate the anisotropy and heterogeneous mechanical properties of lacustrine Triassic Yanchang Formation shale at the microscale (Li et al., 2022; Wang et al., 2022). Also, dynamic fracture growth mechanisms in the Qingshankou shale under compressive failure have been explored (Cai et al., 2022; Meng et al., 2023a), providing valuable insights into its mechanical behavior during deformation. However, limited studies have specifically focused on the varied mechanical behaviors of the bright and dark phases of these oil shale reservoirs (Meng et al., 2023b). Meanwhile, previous studies (Charlton et al., 2023; Szabó et al., 2021; Zhang et al., 2025) commonly employed clustering analysis methods to classify nanoindentation experimental data into mineral categories when investigating the mechanical properties of various minerals. The Gaussian mixture models and K-means algorithms were extensively selected for data fitting and identified different mineral phases from the load-displacement curves (Liu et al., 2022; Yang et al., 2020). However, the widely used traditional clustering methods have certain limitations, resulting in deviations in the clustering analysis outcomes. In the classical method, a probability equation, governing the distribution of test data, is isolated for each mineral component, with no overlap between adjacent populations. As a result, a specified interval is assigned to only one mineral. However, this assumption may not be representative of the inherent variability in rock data (Cavicchia et al., 2022; Madenova and Madani, 2021; Wang et al., 2021). For example, Young's modulus for clay minerals ranges from ~32 to 73.9 GPa, and this interval as 58–90 GPa for calcite (Broz et al., 2006; Kumar et al., 2012; Shukla et al., 2013)—thus, overlapping regions exist. Furthermore, the popular

Gaussian Mixture Model (GMM), employing random and arbitrary distribution ranges for a specific phase, usually results in erroneously covering regions that do not match the actual data. Therefore, an upgraded clustering approach is required to accurately capture the micro-mechanical characteristics of the mixed mineral assembly.

Establishing a robust link between macroscopic, mesoscopic, and microscale mechanical properties of shale is essential in multiscale analysis. Cross-scale correlations between the elastic moduli of individual minerals and mesoscale shale have been established (Wang et al., 2022), providing a rapid and efficient method for characterizing shale mechanical properties. The Mori-Tanaka approach has been widely employed for homogenizing elastic moduli across scales (Chen et al., 1992; Cheng et al., 2025b). Li et al. (2023) adopt the Mori–Tanaka (MT) and the Halpin–Tsai (HT) methods to homogenize the elasticity parameters (elastic modulus and Poisson's ratio) and the hydraulic conductivity of the rock material, respectively. Similarly, Meng et al. (2023a) combined nanoindentation data, K-means clustering, and the Mori-Tanaka method to upscale nanoscale mechanical properties, effectively characterizing shale reservoir heterogeneity. However, current studies rarely address the influence of mineral composition and microstructure on multiscale analysis. In this study, the effect of mineral shape on shale homogenization analysis is explicitly considered, providing a more realistic characterization of the linkage between microscopic and mesoscopic mechanical properties of shale.

The main aim of this work is to analyze the mechanical properties of various minerals through micro-scale measurement and update these to the mesoscale to investigate the mechanical behavior of bright and dark phases of oil shale reservoirs, in general, and in the Ordos Basin in particular. The specific objectives include: (a) investigating the microscale mechanical properties of shale, with particular emphasis on Young's modulus and fracture toughness; (b) developing a novel clustering method to more accurately classify mechanical properties into mineral phases at the micro-scale; and (c) analyzing the anisotropic and heterogeneous characteristics of shale mechanical properties at both micro-scale and mesoscale.

2. Methodology

2.1. Samples

The Ordos Basin, the second-largest lacustrine shale-oil sedimentary basin in China, covers ~250,000 km^2 (Yan et al., 2009). The basin evolved from deposition within a craton depression lake, characterized by a broad, gently sloping, shallow and tectonically stable environment. This environment was highly conducive to the accumulation and storage of oil shale and gas (Lyu et al., 2022), facilitating the deposition of a kilometer-thick sedimentary sequence, composed of river-delta-lake sediments. These sediments are stratigraphically divided into 10 distinct oil-bearing groups, spanning Chang 1 to Chang 10 (Gao et al., 2020; Li et al., 2020). The Chang 7 shale of the Yanchang Formation in the Ordos Basin has shown considerable potential for oil and gas recovery (Han et al., 2021; Zhang et al., 2022) and is stratigraphically subdivided into three sublayers: Chang 7_1, Chang 7_2, and Chang 7_3. In this work, core samples from the Chang 7_2 layer were collected from designated research well JK04, located in Jin Suoguan town, Tongchuan City, in the southern part of the basin. The cores, obtained from depths between 122.57 and 124.99 m, displayed prominent corrugated lamellar structures.

The retrieved cores display alternating bright and dark laminae, indicative of compositional and structural heterogeneity (Fig. 1(a), (b1) and (b2)). To enable micromechanical characterization, two cuboid specimens (8 mm × 8 mm × 3 mm) were extracted using wire-electrode cutting (Fig. 1(b1) and (b2)). The specimens were then prepared for nanoindentation testing in two principal orientations: (i) parallel and (ii) perpendicular to the bedding plane (Fig. 1(c)). A 10 × 10 indentation grid was constructed on the test surface (Fig. 1(d)), with a spacing of 50 μm between adjacent points. This sufficiently large distance minimizes the interaction between neighboring indents, ensuring the accurate acquisition of the sample's micromechanical properties. (Hou et al., 2021; Huang et al., 2025). This layered sampling strategy ensures the representation of intra-layer heterogeneity and enables rigorous evaluation of mineral-phase-dependent mechanical behavior under varying structural orientations, thereby supporting the subsequent multiscale mechanical modeling.

2.2. Equipment

To quantitatively characterize the mineralogical and micromechanical properties of the shale samples, three types of instruments were employed: an X-ray diffractometer (XRD), a Tescan Integrated Mineral Analyzer (TIMA), and an iMicro Nanoindenter. The schematic workflow and corresponding instruments are illustrated in Fig. 2.

XRD was conducted to determine the bulk mineralogical composition of the shale samples (Fig. 2(b)). The operational principle is predicated upon the interaction of incident X-rays with the crystalline lattice of the specimen, resulting in a diffraction pattern that is emblematic of its mineral composition (Kahle et al., 2002). Specific peaks corresponding to minerals were identified to establish the dominant phases. This step provides foundational mineralogical information essential for subsequent mechanical phase classification.

Scanning electron microscopy integrated with energy-dispersive spectroscopy (SEM-EDS), via the TIMA system, was applied to acquire high-resolution mineral mapping at the microscale (Fig. 2(d)). Backscattered electron imaging differentiates mineral phases based on their mean atomic number contrast, while EDS spectra deliver precise elemental composition (Hrstka et al., 2018). By integrating these datasets, individual mineral phases are spatially resolved, enabling the establishment of mineral-structure property correlations.

Instrumented nanoindentation was utilized to measure the micromechanical properties, including hardness and Young's modulus, of the individual mineral phases (Fig. 2(f)). The instrument applies a controlled load to a Berkovich diamond indenter. From the recorded load-displacement curves, mechanical parameters were extracted using the Oliver-Pharr method (Deng et al., 2024; Fischer-Cripps and Nicholson, 2004; Oliver and Pharr, 1992). The separation of loading and unloading stages ensures the decoupling of plastic and elastic responses, enabling accurate mechanical phase differentiation.

Notably, each instrument contributes uniquely to this multiscale investigation: XRD provides the bulk mineralogical composition, TIMA offers spatially resolved mineralogical heterogeneity and structural information, and nanoindentation quantifies the micromechanical properties of the shale samples. The data and properties obtained from each experimental technique are indispensable to the comprehensive understanding of shale behavior across scales.

2.3. Methods

2.3.1. Nanoindentation measurements

We use a 10 × 10 indentation grid over a square area of shale using a Berkovich indenter applied to the material surface via the lattice nanoindentation method (Ulm and Abousleiman, 2006).

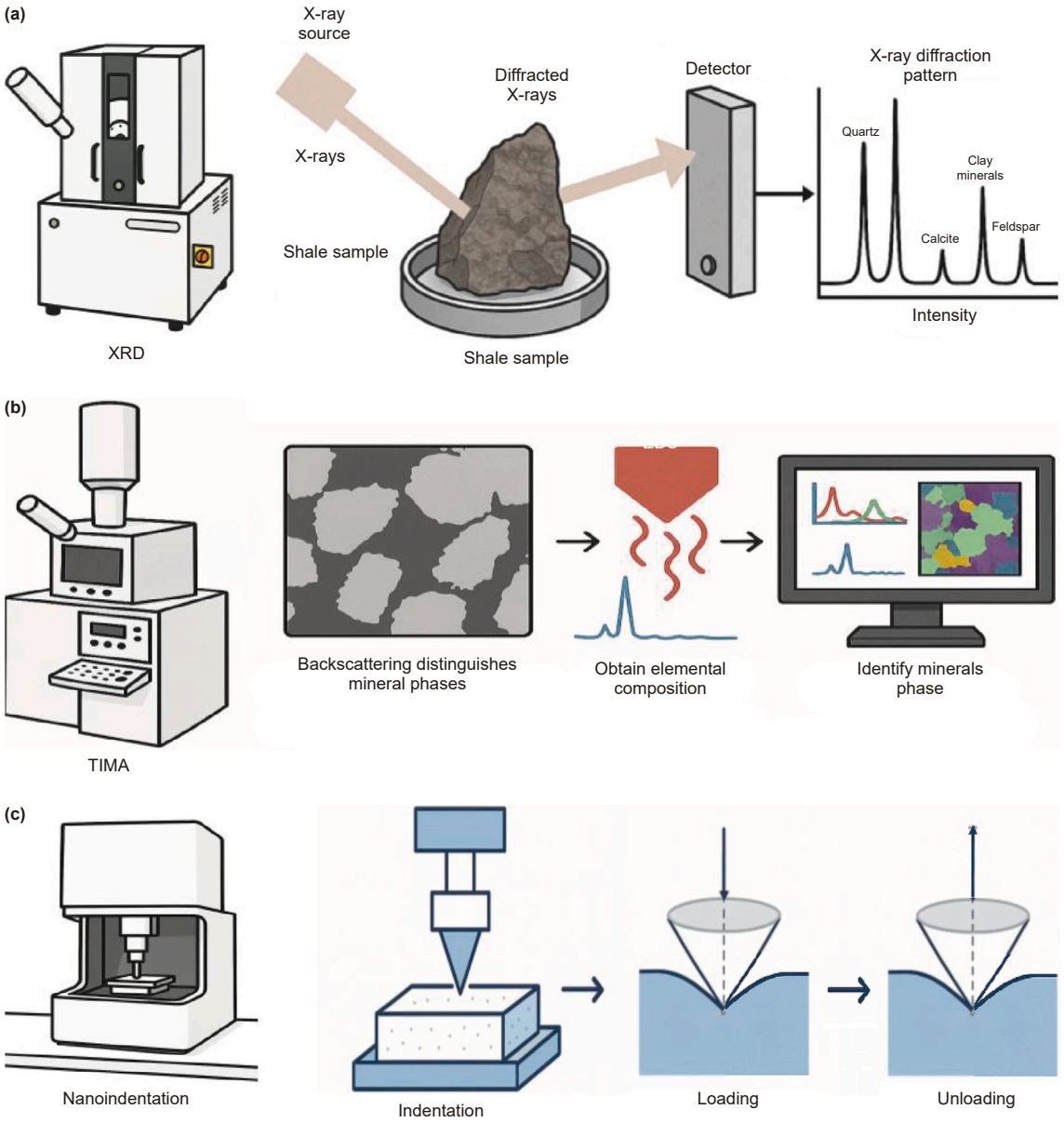

Fig. 2. Experimental equipment. **(a)** XRD experimental principle. **(b)** TIMA experimental principle. **(c)** Nanoindentation experimental principle.

Bedding-parallel and bedding-normal loading orientations were employed to investigate the bright and dark phases of the shale. Therefore, four loading scenarios are categorized as bright bedding-parallel nanoindentation (BBP), bright bedding-normal nanoindentation (BBN), dark bedding-parallel nanoindentation (DBP), and dark bedding-normal nanoindentation (DBN). The nanoindentation testing process consisted of three stages: a loading phase, a holding phase, then an unloading phase. Typical load-indentation depth curves are shown in Fig. 2(d) (Hu and Li, 2015). The displacement-load curve was employed to calculate the Young's modulus and hardness of the minerals within the sample.

The Young's modulus and hardness of the material can be obtained from the value and area of the loading-unloading curves. The hardness is calculated as (Manjunath and Jha, 2019):

$$H = P_m/(A_c \times h_m) \tag{1}$$

where A_c is the indentation contact area, P_m is the maximum load applied during the experiment, and h_m is the maximum displacement during the experiment. On the basis of the elastic energy ratio, the contact stiffness S, which is defined as the slope of the upper part of the quantized unloaded portion (h_m), can be obtained from h_m (Hu and Li, 2015).

$$S = 0.75 \times (2 \times \nu_e - 1) \times P_m/h_m \tag{2}$$

The reduced Young's modulus E_r is then calculated as (Oliver and Pharr, 1992):

$$E_r = (\sqrt{\pi} \times S)\Big/\left(2 \times \sqrt{A_c}\right) \tag{3}$$

Young's modulus of a material, E, can be derived from Eq. (4) (Manjunath and Jha, 2019):

$$1\Big/E_r = \left(1 - \nu^2\right)\Big/E + \left(1 - {\nu_i}^2\right)\Big/E_i \tag{4}$$

where v is Poisson's ratio of the shale sample, v_i is Poisson's ratio of the indenter and E_i is Young's modulus of the indenter.

2.3.2. Fracture toughness measurements

The fracture toughness is also calculated from an energy analysis of the nanoindentation loading curve. The irreversible energy (U_{ir}) is defined as the difference between the total energy (U_t) and the elastic energy (U_e) (Cheng et al., 2002). The mode I stress intensity factor K_{IC} is derived from the critical energy release rate and the reduced Young's modulus as:

$$K_{IC} = \sqrt{G_c \times E_r} \tag{5}$$

where the K represents the stress intensity factor—describing the stress state at the crack tip, subscript "I" indicates a mode-I stress intensity, characterized by tensile opening; while the subscript "c" denotes the critical condition, referring to the value of the stress intensity factor at the onset of crack propagation. G_c is the critical energy release rate, which can be calculated as (Liu et al., 2023):

$$G_c = \partial U_{crack}/\partial A = U_{crack}/A_m \tag{6}$$

The fracture energy (U_{crack}) can be described via Eq. (7):

$$U_{crack} = U_{ir} - U_{pp} \tag{7}$$

where U_{ir} is the irreversible energy generated during the loading process. U_{pp} is pure plastic energy. For the Berkovich indenter employed on this work, the maximum crack area A_m can be calculated as (Liu et al., 2016):

$$A_m = 24.5 \times {h_m}^2 \tag{8}$$

2.3.3. Clustering methods

The data obtained from the nanoindentation test comprised a collection of mineral-specific datasets. In this work, a novel clustering method is employed to proportionally assign and classify each mineral through pre-convolutional and anti-convolutional fitting techniques, which are based on the Gaussian function. This approach aims to categorize the dataset into mineral phases and investigate the variations of micro-mechanical parameters with mineral phases. The Gaussian function is used to simulate the peak values within the dataset with the peak location, width and height determined as (Gauss, 1814):

$$f(x) = a \times \exp\left(-(x-b)^2 \Big/ 2c^2\right) \tag{9}$$

where a is the peak height and b is the center of the curve, that is, the x coordinate where the peak is located. Similarly, c is the width of the Gaussian curve.

Our new methodology comprises two sequential steps: (i) reconstruction of the data space and (ii) application of cluster analysis. Initially, the data obtained from nanoindentation is reorganized into 'interval-count vs. Young's modulus' data pairs. Thereafter, all the data pairs are pre-convolved to obtain the overlapped Gaussian distribution curves (Fig. 3 step (a)), which is the sum of the Gaussian function distribution for an individual phase $f_i(x)$:

$$y(x) = \sum_{i=1}^{5} f_i(x) \tag{10}$$

where i is the representative number of the different mineral phases—clay, quartz, feldspar, dolomite, pyrite. Then, a spatial coordinate system (x-x-y space) is established, with the y-axis designated as the rotation axis and the x-axis serving as the radius. A Gaussian multi-peak surface is obtained through the rotation of the Gaussian curves, obtained by pre-convolution (Fig. 3 step (b)). Subsequently, the anti-convolutional operation (Richardson, 1972) is performed on the Gaussian multi-peaked surface to obtain the probability contour line. In this process, the probability equations are then used to calculate the pointwise probability of each point of the multi-peaked Gaussian surface:

$$p_{a_i}(x) = r_{a_i} \times a_i(x) \tag{11}$$

The normalization factor r_{a_i} is defined as:

$$r_{a_i} = (1/w) \times \int_{k}^{k+w} f_i(x) \Big/ y(x)\mathrm{d}x \tag{12}$$

where k is the starting value of the interval and w is the interval width. As a result, the probability contour map (Fig. 3 step (c)) is determined in the x-x plane by observing the entire Gaussian multi-peak surface along the negative y-axis.

In the clustering process, the data obtained from the nanoindentation test are re-configurated into 'Young's modulus-Young's modulus' data pairs. The data pairs are used to construct the anti-diagonal matrix and subsequently transferred to the input layer (Fig. 3 step (d)) within the data range constrained by the probability contour map. Subsequently, these data are directed to the pooling layer (Fig. 3 step (e)). In this layer, the data in the input layer are randomly allocated into different mineral phases based on the probability contour map obtained during the data reconstruction process. Finally, the processed data are then transferred to the output layer (Fig. 3 step (f)) for visualization and the completion of clustering.

The probability contour map plays a vital role in the entire data processing procedure. Spatially, it defines a square region, constraining the size of the anti-diagonal matrix. At the computing level, it calculates the probability of input data to different mineral phases. The probability is then used in the pooling layer for assignments to data points.

3. Results

3.1. Experimental results

3.1.1. Mineralogical characteristics

Table 1 summarizes the volume fractions of mineral compositions determined via XRD for the bright and dark samples.

The analysis indicates that quartz and clay minerals are the dominant components, constituting >60% of the total composition. The bright samples are predominantly composed of quartz (constituting 51.8%), followed by feldspars (23.7%), exceeding the proportion of clay at 11.3%. Dolomite and pyrite are present at 5.4% and 4%, respectively. In contrast, the dark samples contain a higher proportion of clay minerals (34.4%), surpassing quartz at 28.7%. Pyrite ranked third in the dark samples, accounting for 18%, while feldspars and dolomite are present at 10.7% and 5.1%, respectively. Trace amounts of halite, gypsum, and calcite were also detected, but their concentrations were below the threshold for further discussion in this study.

3.1.2. Microstructural characterization

Tescan integrated mineral analysis (TIMA) was selected to investigate the microstructure of the shale. The mineral surface distribution corresponding to two distinct loading directions, the bright and dark phases, is analyzed and presented in Fig. 4.

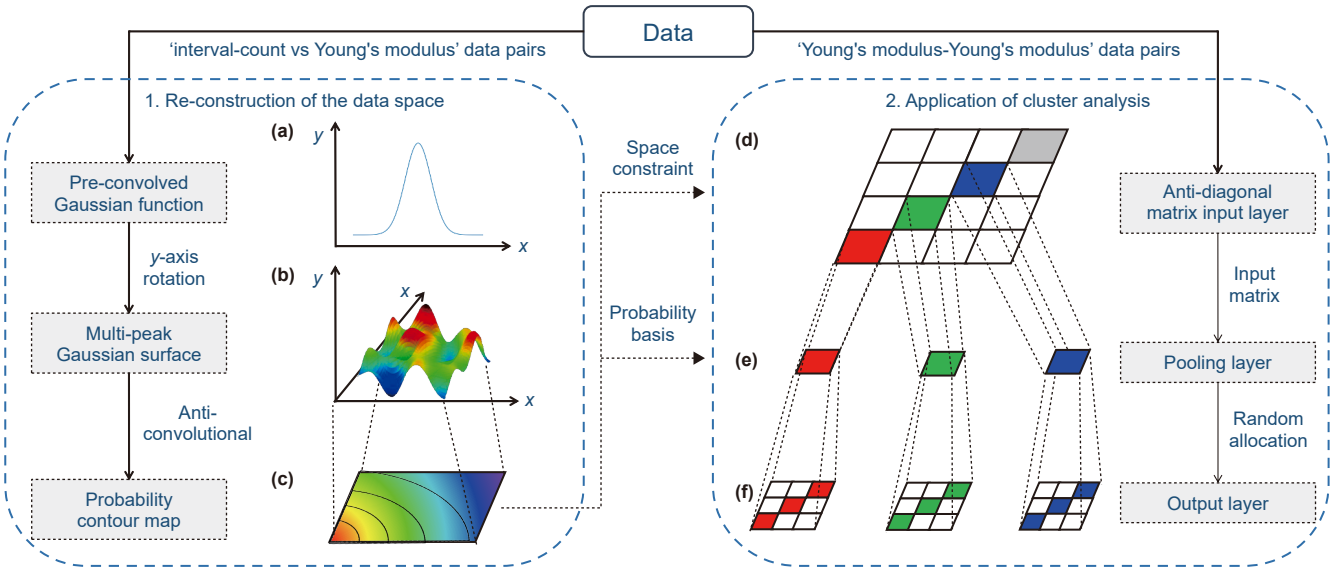

Fig. 3. Schematic diagram of the new clustering method.

Table 1
Composition and proportion of shale in the Ordos region.

	Clay	Quartz	Feldspar	Dolomite	Pyrite	Other
Bright	11.3%	51.8%	23.7%	5.4%	4.0%	3.8%
Dark	34.4%	28.7%	10.7%	5.1%	18%	3.1%

Minerals present in the bright phase samples are distributed in separate blocks, while those in the dark phase samples exhibit a continuous band-like distribution. This observation indicates that the minerals in the bright phase are surrounded by other minerals, whereas the minerals in the dark phase are predominantly surrounded by minerals of the same phase. This exerts significant impact on the disparities in the mechanical properties of minerals of the same type between different phases.

The shape factor can be calculated from the resultant TIMA plot. The shape factor is determined from Eq. (13), which relies on the phase diagram obtained through TIMA, and displayed in Table 2.

$$S_r = \left(\sum_{T=1}^{n} (4\pi \times S_T) \Big/ {L_T}^2 \right) \Big/ n \tag{13}$$

where S_T represents the area of the homogeneous minerals in the TIMA phase diagram, L_T denotes the perimeter of the homogeneous minerals, and n indicates the number of areas where the homogeneous minerals are distinctly identified. The shape factor, which is approximately equal to 1, indicates that the shape of the samples is nearly circular.

3.1.3. Micromechanical measurements

Nanoindentation testing was conducted on a 10 × 10 grid (100 points) for each sample, at an orthogonal grid spacing of 50 μm between each test point. The contact area of each indenter with the exposed surface was ~9 μm^2 (Eq. (8)). The mineral surface and indentation points are illustrated in Fig. 5 demonstrating that all the test points are associated with specific minerals, validating the use of the clustering analysis.

The results are represented as load-displacement curves (Fig. 6), where each curve corresponds to an indentation test, capturing the relationship between the applied load and the resulting displacement. The curves exhibit considerable variability in shape and position, influenced by factors such as the loading direction, mineral composition and microstructural characteristics of the phases. Specifically, the maximum indentation depth, which reflects the material's mechanical response, differs for bright and dark phases due to their distinct mineral compositions and mechanical properties. Additionally, for the same maximum load, the variation in curve slopes and displacements indicate differences in hardness and elastic modulus under different loading conditions.

3.2. Micromechanical analyses

3.2.1. Gaussian curve fitting and clustering

Nanoindentation data points were analyzed using a Gaussian pre-convolution and deconvolution-based clustering method implemented in Python—enabling effective differentiation of minerals within each cluster. Separate clustering analyses were performed for datasets corresponding to different minerals and loading directions, as illustrated in Fig. 7. Table 3 summarizes the result of the mineral composition proportions for each sample. The classification results from the clustering method align closely with the XRD (Table 1) observations, with an overall error of less than 8%. These results highlight the high accuracy and reliability of the proposed clustering approach. However, an exception is observed for pyrite in DBN, where deviations reach up to 10%. These deviations are likely due to the reduced presence of pyrite at the nanoindentation sampling locations. This interpretation is further validated by experimental results for DBN plane samples, where the maximum measured Young's modulus does not exceed 110 GPa (Fig. 7).

Table 4 summarizes the experimental average Young's modulus values and range of Young's modulus for various minerals (clay, quartz, feldspar, dolomite, and pyrite) under different loading conditions. The results show that the measurements are consistent with previous studies, but vary considerably depending on the loading direction and mineral type. These discrepancies are attributed to mineralogical heterogeneity, microstructural features such as interfacial weakening and porosity, and the anisotropic nature of the samples.

3.2.2. Fracture toughness analysis

The fracture toughness at all nanoindentation sampling sites, for each phase and loading direction, was evaluated using Eq. (5).

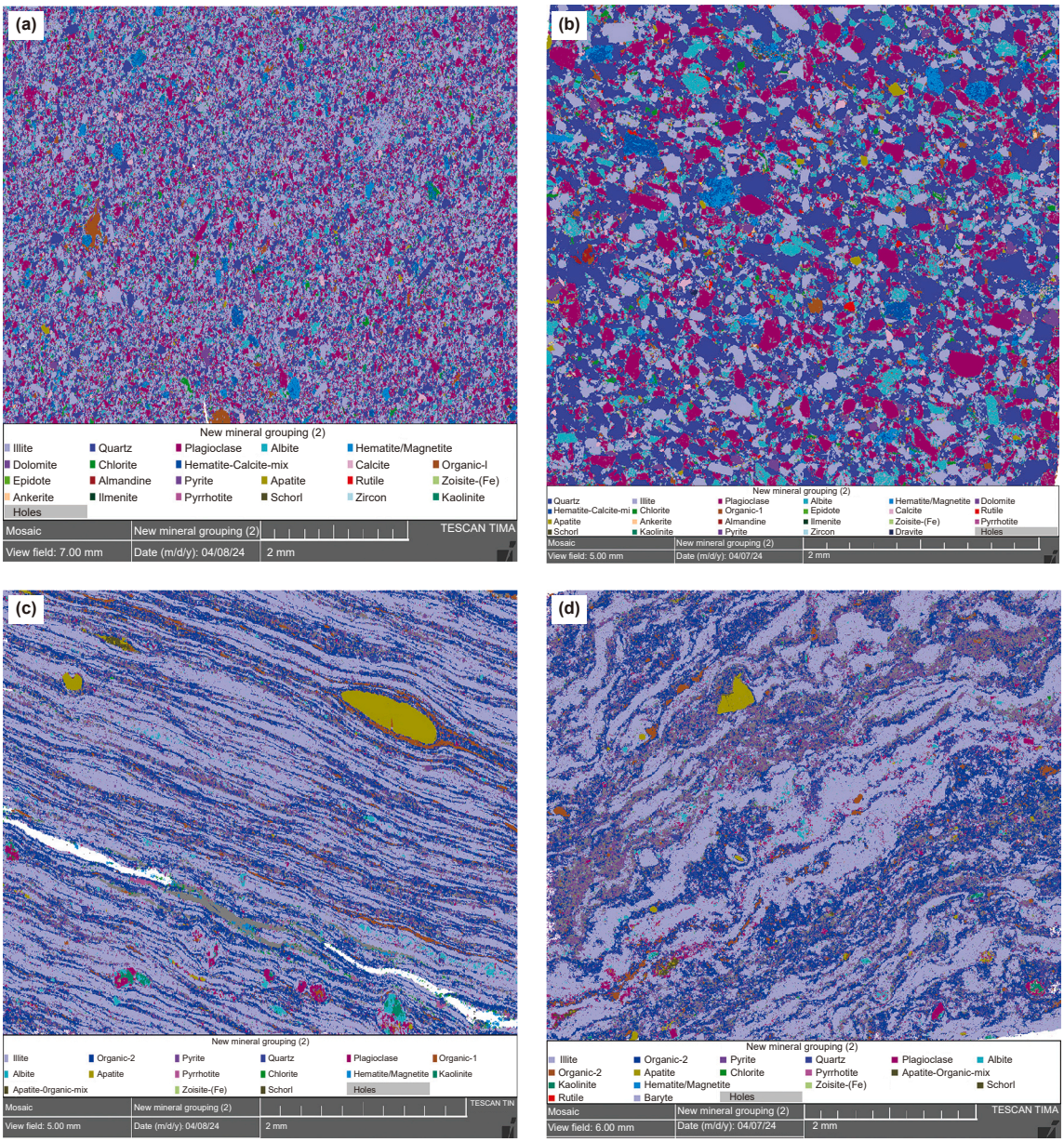

Fig. 4. TIMA experimental surface scanning results. **(a)** Bright bedding-parallel nanoindentation sample (BBP); **(b)** bright bedding-normal nanoindentation sample (BBN); **(c)** dark bedding-parallel nanoindentation sample (DBP); and **(d)** dark bedding-normal nanoindentation sample (DBN).

Table 2
Individual mineral shape factors of the Ordos shale samples.

Sample	Clay	Quartz	Feldspar	Dolomite	Pyrite
BBP	0.92	0.87	0.42	0.60	0.59
BBN	2.16	1.51	0.67	0.95	0.50
DBP	2.72	0.57	0.42	0.46	0.67
DBN	2.62	0.60	0.39	0.47	0.44

BBP: bright bedding-parallel nanoindentation sample; BBN: bright bedding-normal nanoindentation sample; DBP: dark bedding-parallel nanoindentation sample; DBN: dark bedding-normal nanoindentation sample.

Fig. 8 demonstrates a linear relationship between fracture toughness and Young's modulus, independent of the loading direction or phase. While a significant difference in fracture toughness under similar Young's moduli are also observed, indicating the likelihood of mineral mixing. The fracture toughness ranking of the minerals is largely consistent with the sequence of Young's modulus values, from highest to lowest as: pyrite, dolomite, feldspar, quartz, and clay.

The fracture toughness was compared with the values reported in previous studies. The experimental findings reported by Liu et al. (2016) and Liu et al. (2023) indicated fracture toughness values in the range of 0.5–6.5 MPa·m$^{0.5}$, congruent with the range observed in our work.

4. Discussion

4.1. Advantage in upgraded clustering methods

To assess the stability and reproducibility of the novel clustering method, we performed clustering analyses on the BBP dataset three times using Python on different computers, with the

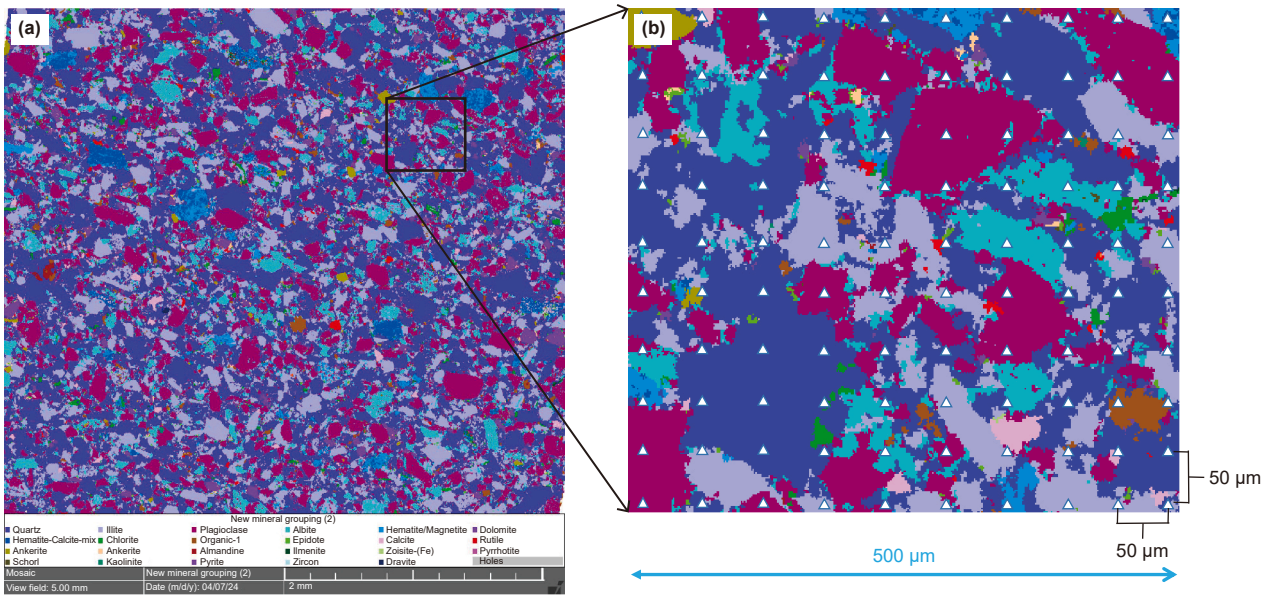

Fig. 5. Experimental surface imaged by TIMA. (**a**) TIMA phase diagram; (**b**) indenter surface contact area schematic.

results presented in Table 5. The clustering outcomes indicate that the results remain highly consistent across multiple runs, including the ranges and count of points in each mineral phase, demonstrating the method's strong stability and reproducibility.

To validate the effectiveness of the upgraded clustering methods, the data obtained from BBP nanoindentation results were also clustered using the K-means clustering method and the Gaussian mixture model (GMM). The clustering results are illustrated in Fig. 9, providing a comparison to demonstrate the advantages of the novel approach. To provide a clearer comparison of the advantages and disadvantages of the three clustering methods, each method is analyzed using the same set of nanoindentation data (BBP) obtained under uniform testing conditions. In this context, the main sources of error in traditional methods arise from the mineralogical characteristics of the same sample, such as the variation in mineral composition, mechanical properties, and structure. Therefore, the method that better adapts to the intrinsic mineralogical properties of the sample will yield more accurate clustering results.

Traditional clustering methods such as K-means and GMM are sensitive to such data fluctuations. In this work, both K-means and Gaussian Mixture Model (GMM) clustering methods exhibit inherent limitations that result in errors when applied to experimental data, particularly data involving complex physical properties. The K-means algorithm assumes hard boundaries between clusters, which leads to misclassification when dealing with overlapping distributions. Fig. 9(a) depicts the results of mineral species classification using the traditional K-means clustering method, where distinct boundaries are evident between varied clusters. This indicates that Young's modulus values obtained from the K-means clustering method are treated as entirely independent with no overlap or intersection, which is inconsistent with the real data. Furthermore, the algorithm is highly sensitive to the initial cluster centroids, which can lead to unstable results, especially when dealing with non-spherical clusters or uneven data distributions.

One major limitation of GMM lies in its sensitivity to the choice of initial parameters and covariance structures. If the covariance matrices are assumed to be equal across clusters, GMM forces each cluster to have the same shape. However, in real data, particularly for materials with varying mineral compositions, the clusters representing different minerals often have distinct shapes and variances. This uniformity assumption leads to errors, especially when mineral distributions are not isotropic or homoscedastic. Fig. 9(b) shows the results of the Gaussian mixture clustering method. This approach effectively addresses the hybridity issue of Young's modulus across various mineral species. However, it also introduces a new challenge. That is, the range of the probability density function for Gaussian mixture clustering method may not be inappropriate for a specific mineral, as the parameters were randomly selected. For example, two outliers, with Young's modulus values exceeding 40 GPa, were incorrectly classified as clay minerals. The innovative method novel in this study addresses the issue of inappropriate evaluation of Young's modulus ranges for a specific mineral existing in the aforementioned methods.

Compared with K-means and GMM, the new approach is better suited to handle overlapping data distributions and can adapt more effectively to experimental uncertainties. The Davies-Bouldin Index (DBI), measuring the average similarity between each cluster and its most similar one (Davies and Bouldin, 1979), is employed as a metric to compare the clustering performance of three methods, as shown in Table 6. A lower DBI value indicates better clustering, featuring distinct and well-separated clusters. Our method exhibits a DBI value slightly higher than that of the K-Means method and slightly lower than that of the GMM. This suggests that the inter-cluster separation and intra-cluster similarity of our approach are somewhat lower than those of K-Means, but its advantage lies in its ability to better handle shale samples with complex anisotropy and multi-phase mineral compositions. Compared to the GMM, our method achieves better separation and clearer cluster boundaries while maintaining higher inter-cluster separation and intra-cluster similarity. Through the novel methods, we are able to finely distinguish between different mineral phases, particularly in terms of mechanical property variations across different bedding orientations, thereby providing more accurate clustering results. The new approach effectively addresses the limitations of traditional clustering methods when applied to multiphase heterogeneous materials, demonstrating higher precision and adaptability.

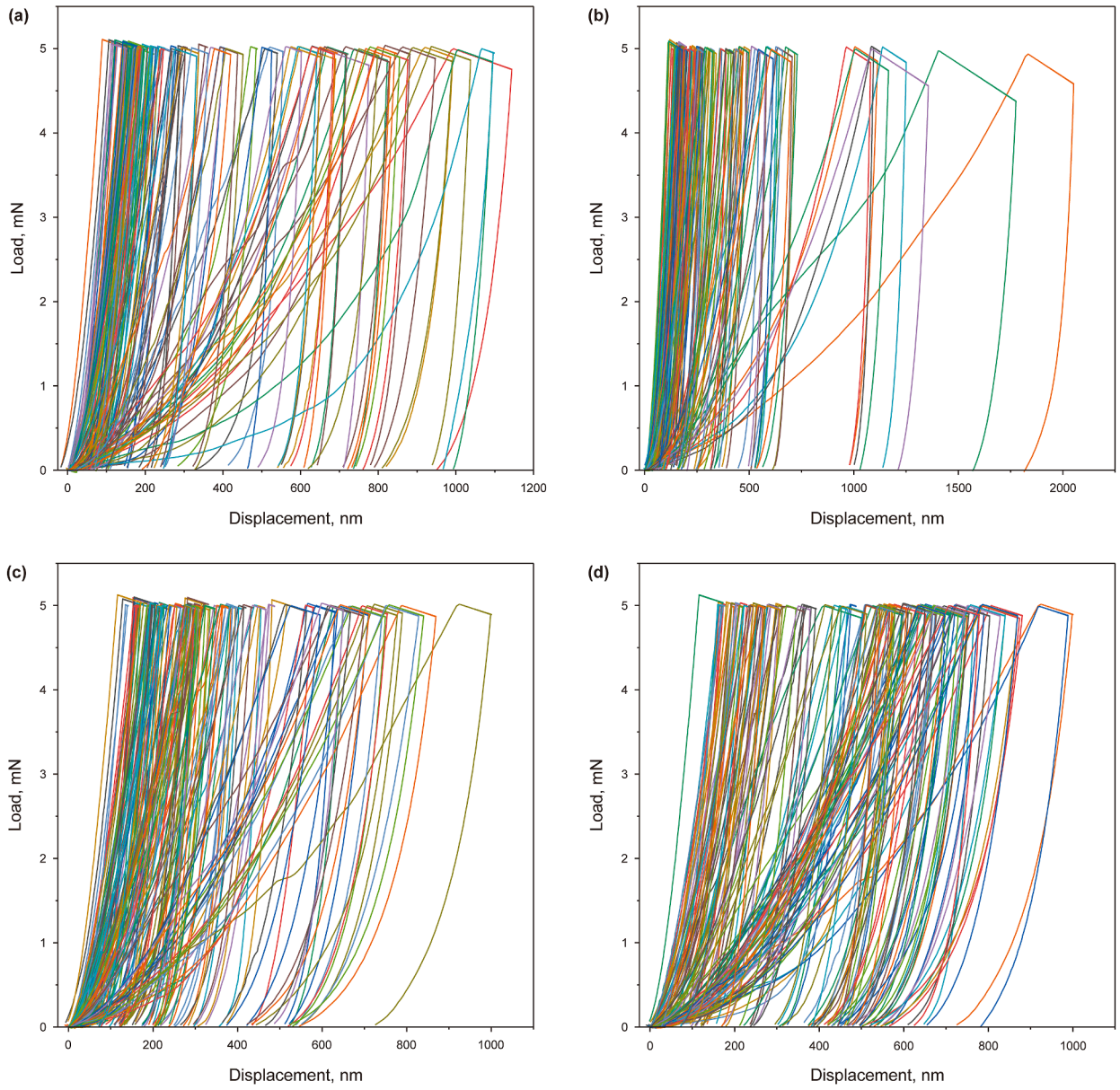

Fig. 6. Nanoindentation test results. **(a)** BBP; **(b)** BBN; **(c)** DBP; and **(d)** DBN.

Through the novel methods, we are able to finely distinguish between different mineral phases, particularly in terms of mechanical property variations across different bedding orientations, thereby providing more accurate clustering results. This approach effectively addresses the limitations of traditional clustering methods when applied to multiphase heterogeneous materials, demonstrating higher precision and adaptability.

4.2. Micromechanical mineralogic anisotropy

This section explores the impact of mineral components on the micromechanical behavior of laminated lacustrine shales. The aim is to clarify the relationships between mineral composition and the observed mechanical properties at the microscale.

4.2.1. Young's modulus

As detected above, the mineral components of the bright and dark phases exhibit significant overlapping similarities. Four permutations are selected for comparison: bright and dark phases, bedding-parallel nanoindentation, and bedding-normal nanoindentation. The results, shown in Fig. 10, reveal that the Young's modulus of BBP and DBP samples (bedding parallel plan) is significantly higher than that of BBN and DBN samples (bedding normal plan). The experimental results consistently demonstrate that Young's modulus of the bright phase is higher than that of the dark phase for the same mineral, regardless of whether the testing direction is parallel or perpendicular to the bedding plane. This trend is validated across all four sample types and is consistently observed for all tested mineral types, including clay, quartz, feldspar, dolomite, and pyrite.

The observed discrepancy in Young's modulus between the bright and dark phases of the shale is attributed to the varied micro-characteristics of shale formed during sedimentation (Chen et al., 2019). Minerals in the dark phase are layered in lamellae, whereas discretely distributed in the bright phase, as shown in Figs. 4 and 11(b). This structural disparity leads to varied

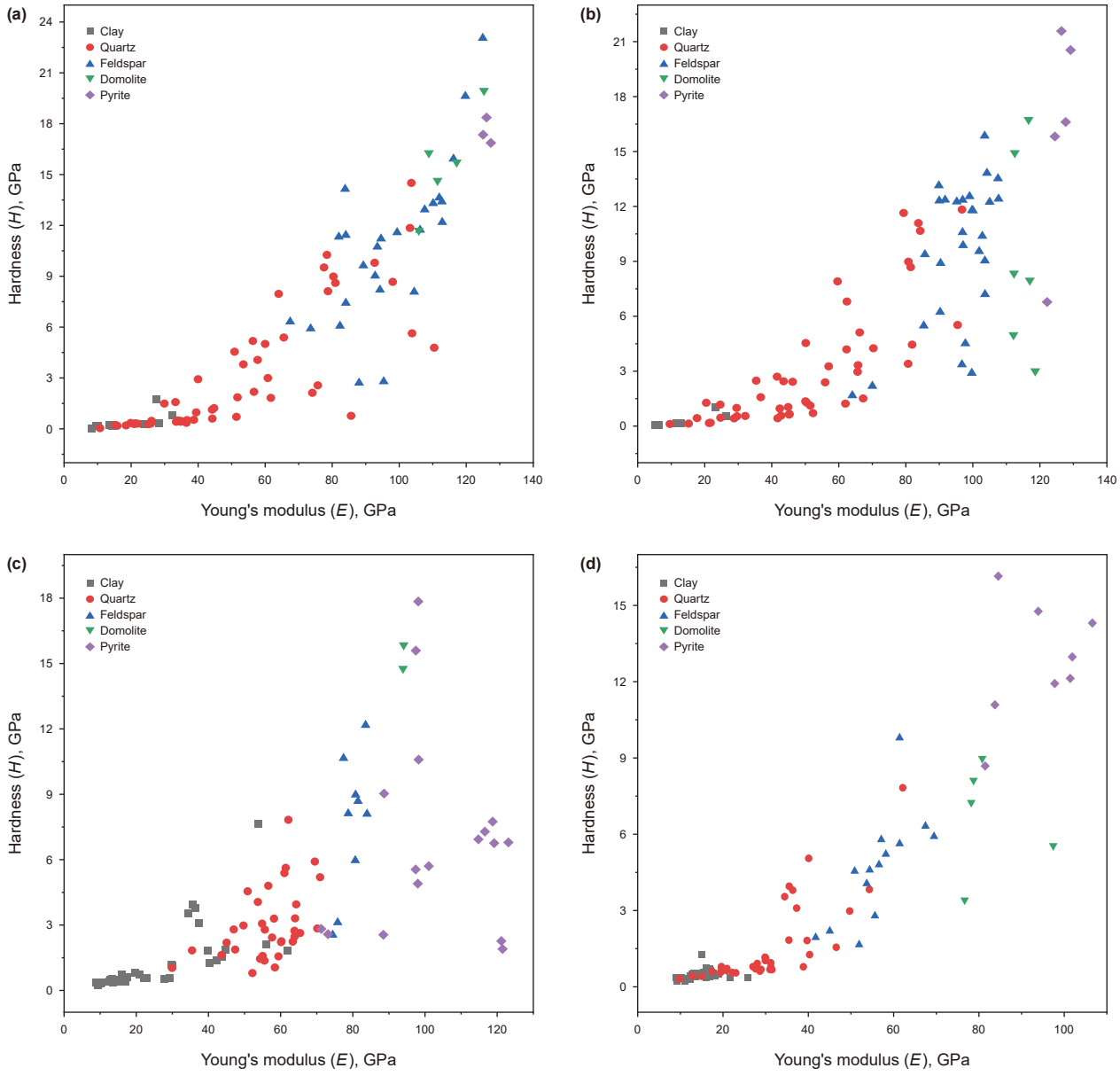

Fig. 7. Clustering results for the Ordos samples. **(a)** BBP; **(b)** BBN; **(c)** DBP; and **(d)** DBN.

Table 3
Percentage of mineral composition of each sample after clustering.

	Clay	Quartz	Feldspar	Dolomite	Pyrite
BBP	10%	52%	25%	5%	3%
BBN	6%	48%	28%	6%	5%
DBP	35%	34%	9%	2%	17%
DBN	37%	36%	14%	5%	8%

deformation responses of the ensemble mineral assemblages in the dark and bright phases to the nanoindentation test and, therefore, to varied micro-mechanical properties. Taking quartz as an example, in the bright phase, quartz is surrounded by isolated hard minerals—feldspars and pyrite (Fig. 11(c1))—which exhibit higher compressive strength and lower deformability. The displacement at the indentation location is smaller (Fig. 11(c2)) because of this boundary constraint, leading to a higher Young's modulus. Conversely, when the probe contacts quartz in the dark phase, a greater displacement is detected due to the underlying softer clay layer. Therefore, a relatively small Young's modulus is returned.

Furthermore, Figs. 4(c), (d) and 11(b) also illustrate that mineral alignment exhibits a more orderly topological structure in the plane parallel to bedding rather than perpendicular to bedding and in the dark phase. This characteristic explains why the Young's modulus is considerably higher in the bedding-parallel direction than in the bedding-normal direction for the dark phase. However, in the bright phase, since mineral alignment shows no significant difference between the two directions (Fig. 4(a) and (b)), the Young's modulus exhibits minimal directional variation.

4.2.2. *Fracture toughness*

A comparative analysis was conducted to evaluate the variation in fracture toughness among different minerals across various groups. Fig. 12 presents the fracture toughness for different minerals in the Ordos bright- and dark-phase samples under different

Table 4
Comparison of the Young's modulus (GPa) of the clustering results for each mineral with the results of previous studies.

	Clay	Quartz	Feldspar	Dolomite	Pyrite
BBP (Average)	18.22	52.19	97.26	113.71	126.14
BBN (Average)	14.33	51.13	85.58	114.86	125.99
DBP (Average)	26.06	56.49	79.65	94.01	102.76
DBN (Average)	14.93	30.96	56.06	82.36	93.92
BBP (Range)	10–32	15–85	82–112	105–125	125–127
BBN (Range)	5–26	29–83	85–107	112–118	122–129
DBP (Range)	8–42	43–71	74–83	93–94	97–121
DBN (Range)	9–26	20–62	50–70	76–97	87–101
Reported	7–20 (Zargari et al., 2011)	55–71 (Eliyahu et al., 2015)	90–100 (Eliyahu et al., 2015)	116.6 (Wang et al., 2001)	250–312 (Mavko et al., 2020)

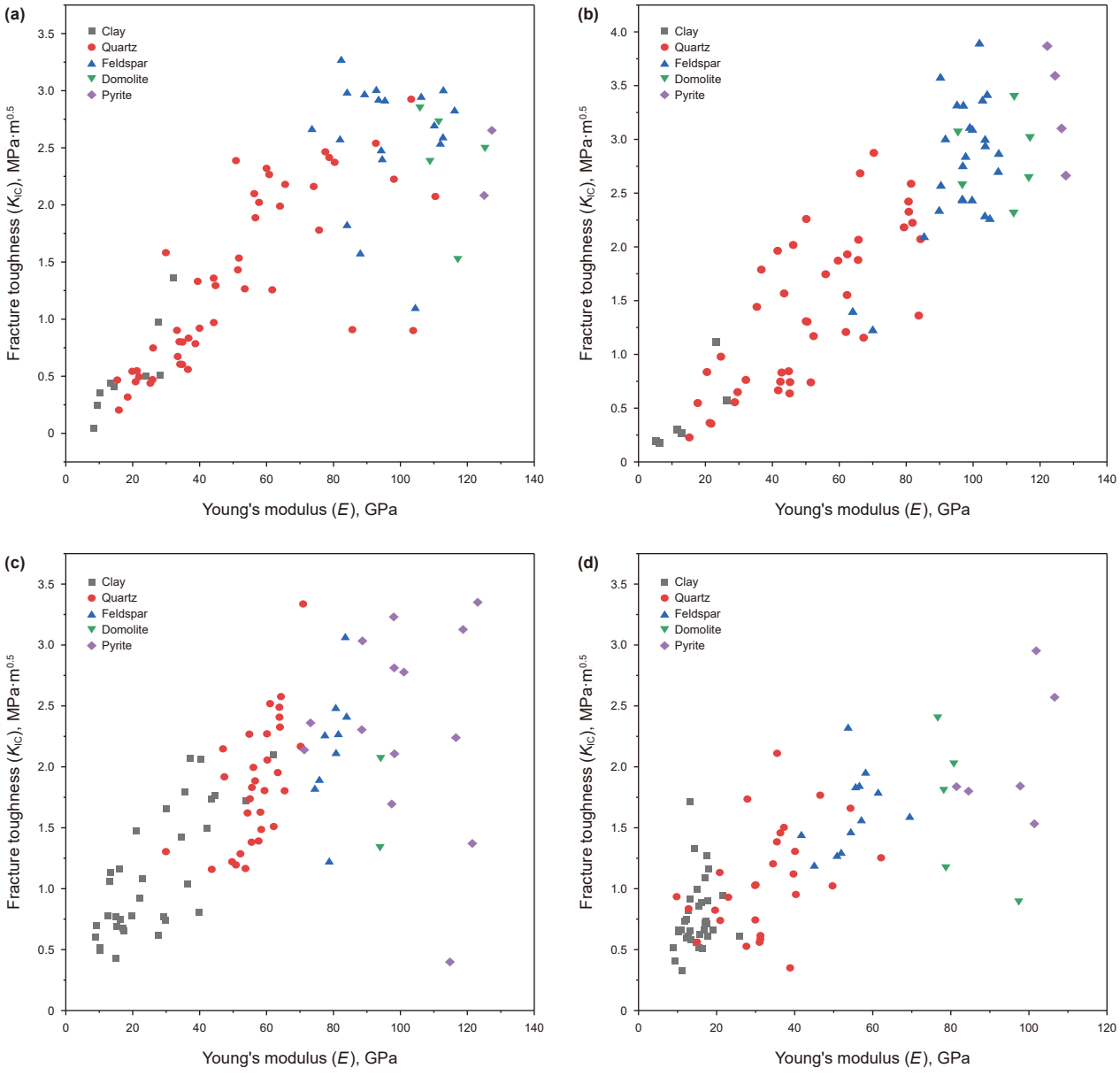

Fig. 8. Fracture toughness results for each mineral test point. **(a)** BBP; **(b)** BBN; **(c)** DBP; and **(d)** DBN.

loading orientations. The plots reveal distinct variations in fracture toughness both between minerals and for different loading directions. Notably, the arrangement of minerals based on fracture toughness closely mirrors that based on Young's modulus, which is primarily attributed to the linear correlation between these two parameters.

In general, fracture toughness for the bright-phase minerals is consistently higher than those for the dark-phase minerals, with bedding-parallel loading resulting in greater fracture toughness compared to bedding-normal loading. However, clay and quartz minerals exhibit an anomaly, with their fracture toughness being greater in the dark phase than in the bright phase. The reason of

Table 5
Young's modulus ranges and data point counts for BBP data across multiple clustering runs.

		Clay	Quartz	Feldspar	Dolomite	Pyrite
First	Range	8.28–32.29	15.87–110.44	81.98–112.73	105.84–125.29	125.03–127.34
	Point counts	10	48	20	7	2
Second	Range	8.28–33.24	15.87–110.44	81.98–110.13	105.84–125.29	125.03–127.34
	Point counts	12	50	19	5	2
Third	Range	8.28–32.29	15.87–110.44	81.98–107.6	105.84–117.15	125.29–127.34
	Point counts	10	51	17	5	3

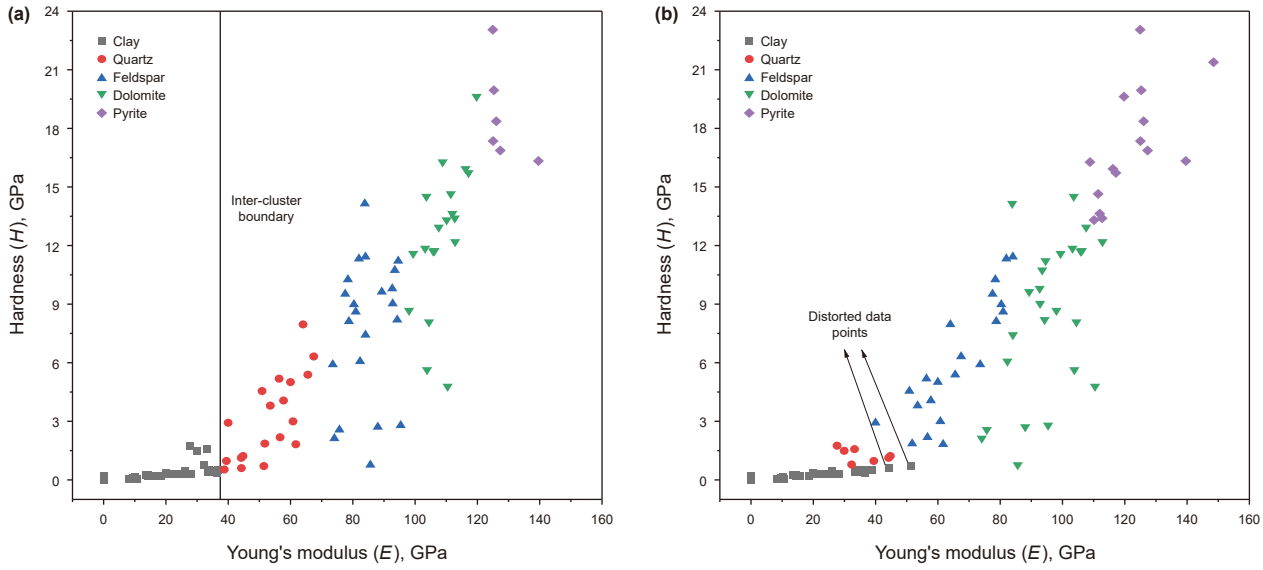

Fig. 9. Traditional clustering results for BBP nanoindentation. **(a)** K-means clustering results; **(b)** GMM clustering results.

Table 6
Clustering performance comparison using DBI for different methods.

DBI	K-means	GMM	This work
BBP	0.53	0.67	0.59
BBN	0.53	0.82	0.69
DBP	0.48	0.47	0.69
DBN	0.43	0.49	0.47

this deviation aligns with the previously discussed discrepancy in Young's modulus, which can be attributed to the effects of deposition and mineral structure. As shown in Fig. 4, the mineral phase diagrams obtained via TIMA reveal that bright-phase minerals (Fig. 4(a) and (b)) are organized as discrete blocks surrounded by other minerals. In contrast, dark-phase minerals (Fig. 4(c) and (d)) form continuous bands, with minerals of similar types adjacent to one another in specific orientations. In the dark phase, clay minerals are arranged in continuous ribbon-like structures that impede crack propagation (Li et al., 2019).

The primary reason for the higher fracture toughness parallel to the bedding laminae compared to the perpendicular direction lies in the mineral alignment along the laminae, which typically follows the sedimentary layering. This parallel arrangement enhances inter-mineral interactions and promotes more uniform stress distribution along the laminae. In contrast, minerals oriented perpendicular to the laminae are more prone to stress concentration. Such stress concentration results in lower fracture toughness and increases the likelihood of fracture.

4.3. Mesoscale—mechanical properties

Following this prior exploration of the micromechanical properties of the Ordos Shale, we address the engineering implications of these mechanical characteristics at the mesoscale. We upscale the nanoindentation data from microscale to mesoscale. The Mori-Tanaka method is the most commonly applied to upscale multiphase elastic composites (Mori and Tanaka, 1973). Within this method, the shale matrix is modeled as a multiphase composite material consisting of a “matrix” phase cushioned within an “envelope” phase region. However, this conventional approach does not fully account for the influence of mineral geometric properties on mechanical behavior. To address this limitation, the mesoscopic Young's modulus of the shale sample regions was recalculated using a modified equation that incorporates shape factor. Table 7 compares the results calculated with and without the inclusion of the shape factor and further contrasts them with previously reported observations (Li et al., 2022; Wang et al., 2022).

In terms of Young's modulus, the incorporation of the shape factor results in a significant reduction for the dark phase samples. This is primarily attributed to the high clay content in the dark phase, which accounts for approximately 80% of the total volume fraction. Since clay has the lowest Young's modulus among the five minerals, the overall modulus is significantly reduced. In contrast, the change in Young's modulus for the bright phase samples is less pronounced. This is because the bright phase contains a higher proportion of quartz and feldspar, which collectively account for 66% of the mineral volume in the parallel direction and 85% in the

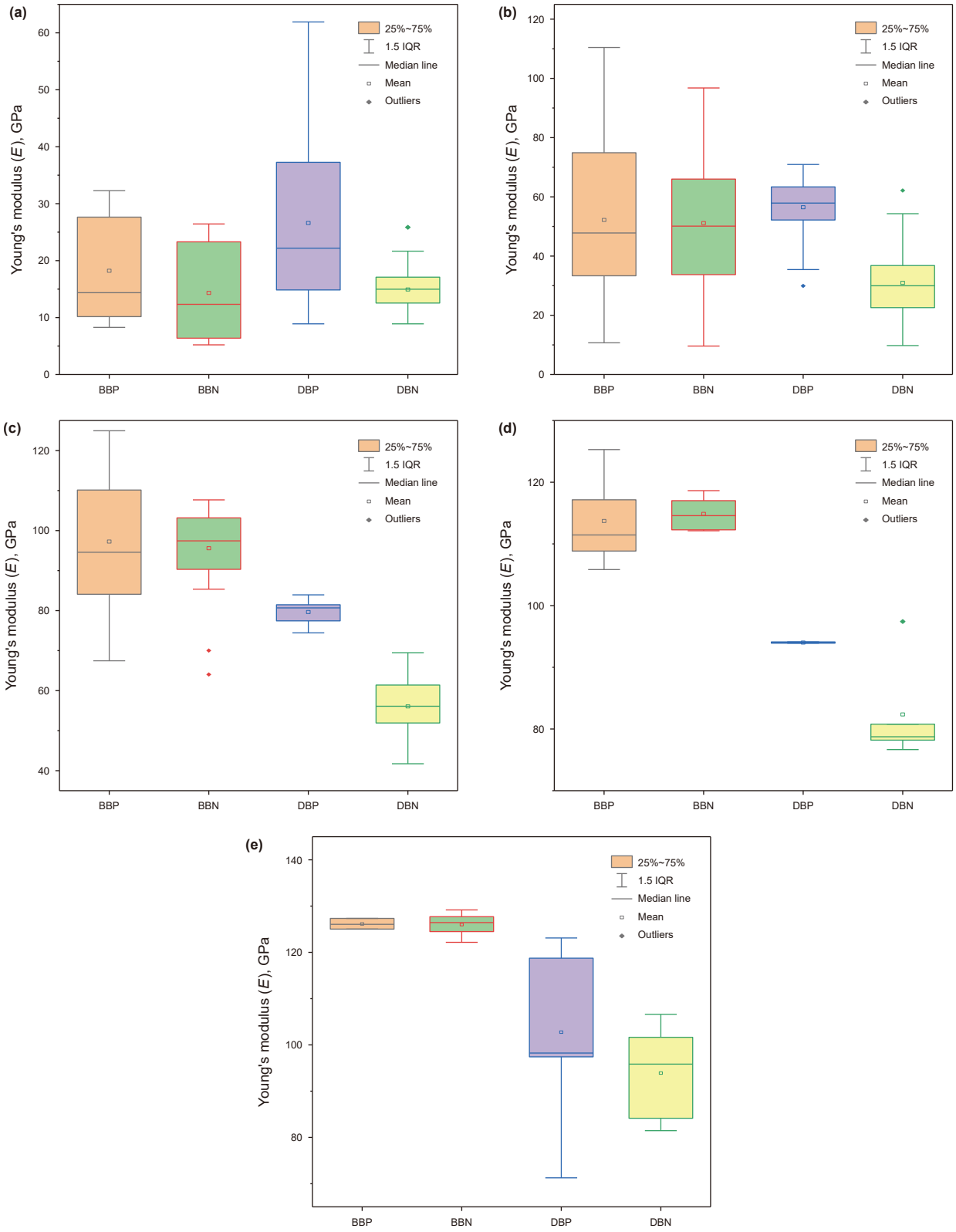

Fig. 10. Young's modulus comparison box plot for component minerals. **(a)** Clay; **(b)** quartz; **(c)** feldspar; **(d)** dolomite; and **(e)** pyrite.

perpendicular direction. As quartz and feldspar have Young's modulus that are intermediate among the five minerals, the overall modulus remains relatively stable despite the inclusion of the shape factor.

The fracture toughness of the Ordos shale remains below 3 MPa·m$^{0.5}$, suggesting that the shales in this region exhibit relatively low brittleness (Gupta et al., 2020). Furthermore, the dark phase samples exhibited a more significant reduction after

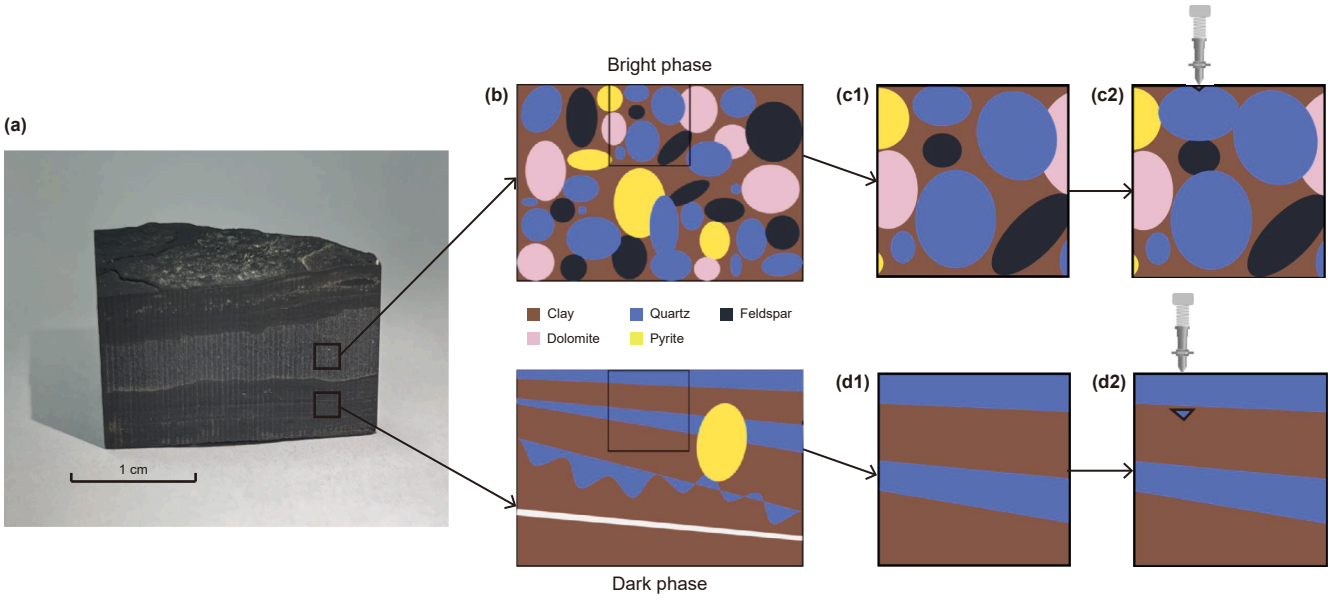

Fig. 11. Schematic illustrating differences in the mechanical characteristics of the same mineral in each of the two different phases and measurement directions caused by deposition and compaction of mineral grains. **(a)** Prismatic sample; **(b)** mineral structure of bright and dark phases; **(c1)** microstructure of bright phase in an unloaded state; **(c2)** microstructure of dark phase in an unloaded state; **(d1)** post-indentation microstructure of bright phase; **(d2)** post-indentation microstructure of dark phase.

incorporating the shape factor, with the bright phase samples showing a smaller change. This can be attributed to the differences in mineral composition and interaction between the two phases. The dark phase, dominated by clay, has inherently lower fracture toughness. The incorporation of the shape factor amplifies the effect of the weak-layered structure of clay, leading to a marked reduction in toughness. Conversely, the bright phase contains a higher proportion of hard minerals, such as quartz and feldspar, with higher and more uniform fracture toughness. As a result, the impact of the shape factor is less pronounced for the bright phase, leading to relatively minor changes in fracture toughness.

The Young's modulus of the oil shale reservoirs of the Ordos Basin is 41.39 GPa in bedding-parallel direction and 35.65 GPa in the bedding-normal, at the sample scale, as measured by Li et al. (2022) with the value of fracture toughness 1.49 MPa·m$^{0.5}$ bedding-parallel and 1.32 MPa·m$^{0.5}$ bedding-normal. These values, obtained through the shape factor (Table 7), more closely approximate the actual measured values, primarily because the integration of the shape factor in the homogenization analysis better represent the geometric characteristics of minerals.

The anisotropy of the shale in this study is compared with that of shales from other regions, and Table 8 summarizes the macro-scale Young's modulus anisotropy ratios R for several regions. As seen in Table 8, the R values vary widely, ranging from 1.2 for the Chicopee shale to 2.5 for the Chattanooga shale. Clearly, the R values determined in this study, for both the bright and dark phases, fall within a relatively low range compared to those from other regions. Upon comparing the anisotropy ratios between the bright and dark phases, it can be observed that the R values for the dark phase of the Ordos sample are significantly higher than those for the bright phase. This is mainly attributed to the high anisotropy of clay minerals, which have a pronounced impact on the overall anisotropy of shale at the microscale, thereby influencing its macroscopic anisotropic characteristics.

While this study focuses on the micro-mechanical properties of shale samples and the upscaling process, it does not include Finite Element Analysis (FEA), which is widely utilized in understanding scale-dependent effects (Alzebdeh and Ostoja-Starzewski, 1996; Danielli et al., 2023). FEA has played a crucial role in simulating the stress-strain behavior of materials under various loading conditions, offering deeper insights into their mechanical performance (Lichinchi et al., 1998; Sami Ullah Khan and Wasim Jamshed, 2023). For instance, Tricarico and Tan (2022) employed finite element (FE) simulations in combination with nano-indentation experiments to develop an appropriate constitutive model and determine a more accurate estimate of the yield stress.

4.4. Implications at field scale

This study highlights the variation in the mechanical properties of shale across length scales and phases, which plays a vital role in guiding the response in shale reservoirs. Porosity and permeability are identified as critical parameters in evaluating shale oil reservoirs, showing a clear correlation with Young's modulus (Cui et al., 2018; Sone and Zoback, 2013). Bright-phase minerals, characterized by higher rigidity and lower porosity, may limit gas transport capacity, with the higher porosity of the dark-phase minerals enhancing gas storage and then release. The clay-rich dark phase exhibits greater deformability, rendering its pore structures more prone to alteration or collapse during gas depletion and consequently reducing reservoir permeability. In contrast, minerals such as quartz, feldspar, dolomite and pyrite reflect a higher Young's modulus, exhibiting a more stable pore structure with lower compressibility. This stability reduces the stress sensitivity of shale reservoirs, maintaining high porosity and permeability under increased effective stress and enhancing shale oil recovery.

Fracture toughness partly controls the hydraulic fracturing behavior of oil shale reservoirs (Gale et al., 2007). Our study reveals that the fracture toughness of the bright phase is higher than that of the dark phase, suggesting a greater resistance to both the initiation of new fractures and propagation of current fractures through the bright phase. In contrast, the lower toughness of the dark phase makes it more prone to fracture propagation under the same fracturing pressures (Sun et al., 2024). In other words, the hydraulic fracture is more likely to terminate in the bright phase and to continue through the dark phase. These findings highlight

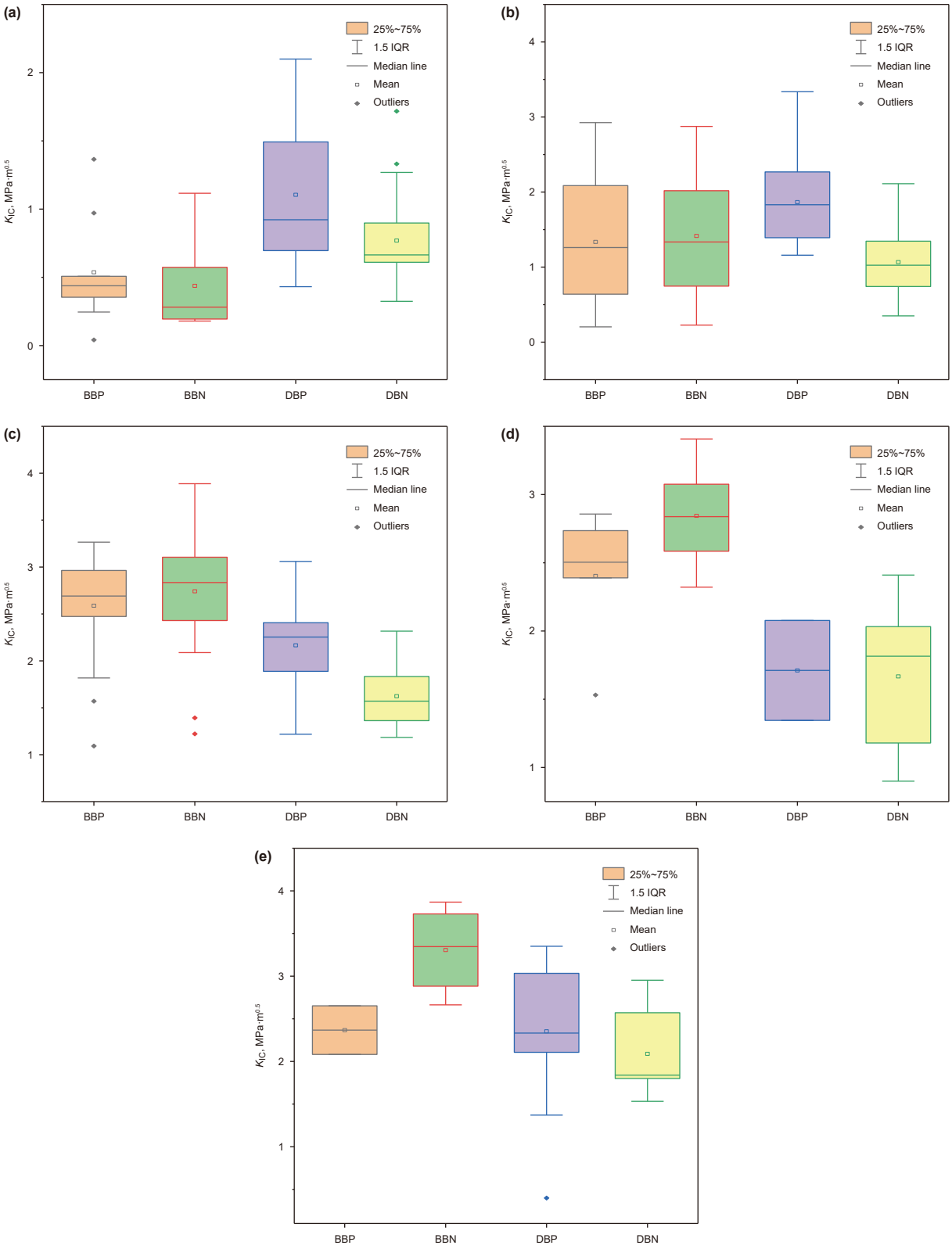

Fig. 12. Boxplot of fracture toughness comparison for each mineral. Different components minerals are **(a)** clay; **(b)** quartz; **(c)** feldspar; **(d)** dolomite; and **(e)** pyrite.

the significance of customizing fracturing strategies in field engineering to consider variations in fracture toughness related to different stratigraphic structures in shale formations (Cui et al., 2020).

The variations in Young's modulus and fracture toughness across different scales indicate significant scale effects on the mechanical properties of shale. The higher Young's modulus and fracture toughness at the microscale compared to those at the

Table 7
Comparison of Young's Modulus and fracture toughness of shale minerals considering shape factor effects relative to previous results.

		BBP	BBN	DBP	DBN	BP	BN
Young's Modulus, GPa	Without shape factor	93.33	92.80	77.50	63.63	41.39 (Li et al., 2022)	35.65 (Li et al., 2022)
	With shape factor	66.05	70.29	39.26	22.18		
K_{IC}, MPa·m$^{0.5}$	Without shape factor	1.68	2.56	2.14	1.69	1.49 (Wang et al., 2022)	1.32 (Wang et al., 2022)
	With shape factor	1.41	2.23	1.52	0.99		

In the table, BP represents the bedding parallel plane, and BN denotes the bedding-normal plane.

Table 8
Macroscopic anisotropy ratios of shale from various regions.

Shale	anisotropy ratios R	Reference
Ordos bright simple	1.1	This work
Ordos dark simple	1.8	This work
Chicopee	1.2	Lo et al. (1986)
Longmaxi	1.4	Lin et al. (2017)
New Albany	1.8	Johnston and Christensen (1995)
Boryeong	2.1	Cho et al. (2012)
Chattanooga	2.5	Johnston and Christensen (1995)

mesoscale indicate that shale exhibits greater rigidity and toughness within fine structures or at the nanopore level. These findings emphasize the importance of considering scale-dependent effects during reservoir simulations and in designing exploitation strategies. By incorporating scale effects into predictive models, the accuracy of deformation and fracture behavior assessments can be improved, thereby enhancing the reliability and efficiency of shale reservoir development plans.

4.5. Limitations and future work

4.5.1. Limitations

Several limitations of this study warrant acknowledgment. (i) The applicability and local optimality of the newly developed clustering method for measured data classification is constrained. A Gaussian distribution is specified in the new approach and this assumption may not adequately represent the configuration of mechanical properties of a certain mineral. Furthermore, the results obtained through Gaussian pre-convolution lack global optimality and may introduce computational imprecision. To mitigate this limitation, future work can focus on enhancing the generalizability of the clustering model, potentially incorporating more advanced statistical techniques or hybrid methods to better accommodate the diverse distribution of mineral properties. For example, Through the application of big data analytics to optimize the adaptation of micro-mechanical parameters across various minerals, combined with deep learning approaches for improved classification accuracy. (ii) Mechanical characteristics at the mesoscale may not be fully captured. Although a micro-mechanical test and a n0ovel scaling method with a correction term were employed, the pores and fractures within the oil shale formation have been overlooked. (iii) Experimental conditions were limited to nanoindentation tests on dry samples at room temperature. These conditions do not account for in situ environmental factors, such as elevated in situ temperatures and water saturation, which likely influence the mechanical properties of shale.

4.5.2. Future work

Based on the identified limitations, the following suggestions are proposed for future research: (i) Improvement in the accuracy and efficiency of the clustering method is urgently needed. Current clustering methods, utilizing Gaussian pre-convolution and inverse convolution, categorize extensive measurement data into mineral groups with relatively high accuracy. However, advanced classification techniques are required to further enhance both accuracy and computational efficiency. (ii) Effort should also be focused on accurately describing reservoir characteristics after scale upgrading. This includes incorporating features such as natural fractures, large pores and other unique geological attributes to refine upscaling methods to reservoir scale. (iii) Replicating the reservoir environment is critical for the measurement. Nanoindentation tests should be conducted under conditions that simulate the in-situ reservoir environment, including thermal conditions and pre-immersion of samples in water to reflect varying water saturations. (iv) Future work could incorporate Finite Element Analysis (FEA) to simulate the stress–strain behavior of shale at multiple scales, providing deeper insights into scale-dependent mechanical responses and aiding in the validation of constitutive models derived from experimental and deep learning approaches.

5. Conclusions

We performed nanoindentation testing on laminated lacustrine shales to evaluate mechanical properties at the microscopic scale and on bedding faces and perpendicular to bedding. The resulting data were categorized into distinct mineral phases, using a novel clustering technique. A shape factor derived from TIMA was then incorporated into the upgraded Mori-Tanaka method, facilitating effective upscaling of mechanical properties from microscale to mesoscale. The key conclusions of this research are summarized as follows.

(i) An upgraded clustering technique, utilizing Gaussian pre-convolution and anti-convolution, is developed and applied to establish the relationship between micro-mechanical properties and mineral compositions. The upgraded clustering method has demonstrated highly consistent clustering results in multiple runs, proving its excellent stability and repeatability when dealing with complex measured data. This new approach effectively addresses the limitations of traditional K-means clustering, which assumes mutually exclusive clusters, and GMM clustering, which is prone to delineating incorrect mineral ranges.

(ii) The elastic properties of the shale matrix display anisotropy and heterogeneity at the micro-scale. The bright phase, featuring discrete hard minerals, limits deformation during nanoindentation and results in a higher Young's modulus, reducing the stress sensitivity of shale reservoirs, maintaining initial porosity and permeability; While lower Young's modulus in clay-rich dark phase increases deformability, making pore structures more likely to alter or collapse, thus reducing reservoir permeability during the gas depletion process. Also, the property of the dark phase is significantly greater in the bedding-parallel direction than in the bedding-normal direction due to more orderly

alignment, while little difference is observed in the bright phase.

(iii) Fracture toughness varies significantly among minerals and directions, with bright-phase minerals generally exhibiting higher toughness than dark-phase minerals, and loading along the bedding-parallel plane resulting in greater fracture toughness compared to that in the bedding-normal plane. The alignment of minerals along sedimentary laminae enhances inter-mineral interactions and elevates stress distribution, leading to higher fracture toughness in the bedding-parallel plane compared to the bedding-normal plane. The varied fracture toughness among minerals makes hydraulic fracture more prone to penetrate in dark phase and terminate in the bright phase.

(iv) The Young's modulus and fracture toughness at the meso-scale can be determined through the Mori-Tanaka method, incorporating a shape factor. The acquired value is lower than that obtained through the classical method and the value at a micro scale, and aligns more closely with the actual results of the triaxial test. The inconsistencies observed across various scales suggest that shale demonstrates enhanced rigidity and toughness at the nanopore level. The developments of more accurate classification algorithms, advanced upscaling techniques, experimental protocols and finite element analysis that better simulate in-situ conditions are urgently needed for future studies.

CRediT authorship contribution statement

Zi-Geng Pei: Conceptualization, Writing – original draft, Visualization, Software. **Guang-Lei Cui:** Supervision, Funding acquisition, Conceptualization. **Yong-Ting Duan:** Writing – review & editing, Validation, Funding acquisition. **Yu-Ling Tan:** Resources, Methodology, Data curation. **Derek Elsworth:** Writing – review & editing, Supervision, Conceptualization. **Wang-Xing Cheng:** Visualization, Data curation. **Ning-Liang Sun:** Project administration, Funding acquisition. **Zhe-Jun Pan:** Formal analysis, Conceptualization.

Declaration of competing interest

The authors declare that they have no known competing financial interests or personal relationships that could have appeared to influence the work reported in this paper.

Acknowledgments

The research delivered partial results under supports of the by the National Natural Science Foundation of China (Grant No. 12002081, No. 42102309), and Natural Science Foundation of Hebei (No. D2024501002), and 111 Project (No. B17009). DE gratefully acknowledges support from the G. Albert Shoemaker endowment.

References

Alzebdeh, K., Ostoja-Starzewski, M., 1996. Micromechanically based stochastic finite elements: length scales and anisotropy. Probabilistic Eng. Mech., Third International Stochastic Structural Dynamics Conference 11, 205–214. https://doi.org/10.1016/0266-8920(96)00015-X.

Bohacs, K.M., Carroll, A.R., Neal, J.E., Mankiewicz, P.J., 2000. Lake-Basin Type, Source Potential, and Hydrocarbon Character: An Integrated Sequence-Stratigraphic–Geochemical Framework.

Broz, M.E., Cook, R.F., Whitney, D.L., 2006. Microhardness, toughness, and modulus of Mohs scale minerals. Am. Mineral. 91, 135–142. https://doi.org/10.2138/am.2006.1844.

Cai, J.C., Zhao, L.X., Zhang, F., Wei, W., 2022. Advances in multiscale rock physics for unconventional reservoirs. Adv. Geo-Energy Res. 6, 271–275.

Cavicchia, C., Vichi, M., Zaccaria, G., 2022. Gaussian mixture model with an extended ultrametric covariance structure. Adv. Data Anal. Classif. 16, 399–427. https://doi.org/10.1007/s11634-021-00488-x.

Chalmers, G.R., Bustin, R.M., Power, I.M., 2012. Characterization of gas shale pore systems by porosimetry, pycnometry, surface area, and field emission scanning electron microscopy/transmission electron microscopy image analyses: examples from the Barnett, Woodford, Haynesville, Marcellus, and Doig units. AAPG Bull. 96, 1099–1119. https://doi.org/10.1306/10171111052.

Charlton, T.S., Rouainia, M., Aplin, A.C., Fisher, Q.J., Bowen, L., 2023. Nano-indentation of horn river basin shales: The micromechanical contrast between overburden and reservoir formations. J. Geophys. Res. Solid Earth 128, e2022JB025957. https://doi.org/10.1029/2022JB025957.

Chen, T.Y., Dvorak, G.J., Benveniste, Y., 1992. Mori-tanaka estimates of the overall elastic moduli of certain composite materials. J. Appl. Mech. 59, 539–546. https://doi.org/10.1115/1.2893757.

Chen, Y.H., Zhu, Z.W., Zhang, L., 2019. Control actions of sedimentary environments and sedimentation rates on lacustrine oil shale distribution, an example of the oil shale in the Upper Triassic Yanchang Formation, southeastern Ordos Basin (NW China). Mar. Pet. Geol. 102, 508–520. https://doi.org/10.1016/j.marpetgeo.2019.01.006.

Cheng, W.X., Cui, G.L., Elsworth, D., Tan, Y.L., Pan, Z.J., Guo, Y.J., Zhang, Y., 2025a. Constrained study of nanoindentation-based upscaling of mechanical properties of shales. Acta Geotech 20, 4515–4533. https://doi.org/10.1007/s11440-025-02663-2.

Cheng, W.X., Guo, Y.J., Cui, G.L., Elsworth, D., Tan, Y.L., Pan, Z.J., 2025b. Impact of micro-scale characteristics of shale reservoirs on gas depletion behavior: A microscale discrete model. Adv. Geo-Energy Res. 15, 143–157.

Cheng, Y.T., Li, Z.Y., Cheng, C.M., 2002. Scaling relationships for indentation measurements. Philos. Mag. A 82, 1821–1829.

Cho, J.-W., Kim, H., Jeon, S., Min, K.-B., 2012. Deformation and strength anisotropy of Asan gneiss, Boryeong shale, and Yeoncheon schist. Int. J. Rock Mech. Min. Sci. 50, 158–169. https://doi.org/10.1016/j.ijrmms.2011.12.004.

Cui, G.L., Liu, J.S., Wei, M.Y., Shi, R., Elsworth, D., 2018. Why shale permeability changes under variable effective stresses: New insights. Fuel 213, 55–71. https://doi.org/10.1016/j.fuel.2017.10.068.

Cui, G.L., Feng, X.T., Pan, Z.J., Chen, T.Y., Liu, J., Elsworth, D., Tan, Y., Wang, C., 2020. Impact of shale matrix mechanical interactions on gas transport during production. J. Pet. Sci. Eng. 184, 106524. https://doi.org/10.1016/j.petrol.2019.106524.

Danielli, F., Ciriello, L., La Barbera, L., Rodriguez Matas, J.F., Pennati, G., 2023. On the need of a scale-dependent material characterization to describe the mechanical behavior of 3D printed Ti6Al4V custom prostheses using finite element models. J. Mech. Behav. Biomed. Mater. 140, 105707. https://doi.org/10.1016/j.jmbbm.2023.105707.

Davies, D.L., Bouldin, D.W., 1979. A cluster separation measure. IEEE Trans. Pattern Anal. Mach. Intell. PAMI-1, 224–227. https://doi.org/10.1109/TPAMI.1979.4766909.

Deng, H.F., Huang, Y.N., Xiao, Y., Xu, P.F., Li, J.L., Wang, M.Y., 2024. Study on the time delay failure characteristics of sandstone unloading under dynamic disturbance. Deep Resour. Eng 1, 100114. https://doi.org/10.1016/j.deepre.2024.100114.

Duan, Y.T., Zhu, C.C., Yang, B.C., Kong, R., Gu, L.J., Li, Y., 2024. Fracture propagation and failure mode characteristics of lamellar lacustrine shale under true triaxial compression conditions. Environ. Earth Sci. 83, 96. https://doi.org/10.1007/s12665-023-11390-4.

Eliyahu, M., Emmanuel, S., Day-Stirrat, R.J., Macaulay, C.I., 2015. Mechanical properties of organic matter in shales mapped at the nanometer scale. Mar. Pet. Geol. 59, 294–304.

Evans, A.G., 1990. Perspective on the development of high-toughness ceramics. J. Am. Ceram. Soc. 73, 187–206. https://doi.org/10.1111/j.1151-2916.1990.tb06493.x.

Fischer-Cripps, A.C., Nicholson, D.W., 2004. Nanoindentation. Mechanical engineering series. Appl. Mech. Rev. 57, B12. B12.

Fu, J.H., Li, S.X., Niu, X.B., Deng, X.Q., Zhou, X.P., 2020. Geological characteristics and exploration of shale oil in Chang 7 member of triassic Yanchang Formation, Ordos Basin, NW China. Petrol. Explor. Dev. 47, 931–945.

Gale, J.F.W., Reed, R.M., Holder, J., 2007. Natural fractures in the Barnett Shale and their importance for hydraulic fracture treatments. AAPG Bull. 91, 603–622. https://doi.org/10.1306/11010606061.

Gao, Y.H., Feng, X.T., Wang, Z.F., Zhang, X.W., 2020. Strength and failure characteristics of jointed marble under true triaxial compression. Bull. Eng. Geol. Environ. 79, 891–905. https://doi.org/10.1007/s10064-019-01610-2.

Gauss, C.F., 1814. Methodus Nova Integralium Valores Per Approximationem Inveniendi.

Guo, W., Deng, S.H., Sun, Y.H., 2024. Recent advances on shale oil and gas exploration and development technologies. Adv. Geo-Energy Res. 11, 81–87.

Gupta, I., Sondergeld, C., Rai, C., 2020. Fracture toughness in shales using nano--indentation. J. Pet. Sci. Eng. 191, 107222. https://doi.org/10.1016/j.petrol.2020.107222.

Han, T.C., Yu, H.Y., Fu, L.Y., 2021. Correlations between the static and anisotropic dynamic elastic properties of lacustrine shales under triaxial stress: Examples from the Ordos Basin, China. Geophysics 86, MR191–MR202. https://doi.org/10.1190/geo2020-0761.1.

Hou, L.H., Lin, S.H., Zhang, L.J., 2021. New insights from geostatistics on the genetic relationship between shales, mudstones, and sandstones within a parasequence in the lower Chang7 Member of the Upper Triassic Yanchang Formation, Ordos Basin, Northern China. J. Asian Earth Sci. 213, 104767. https://doi.org/10.1016/j.jseaes.2021.104767.
Hrstka, T., Gottlieb, P., Skala, R., Breiter, K., Motl, D., 2018. Automated mineralogy and petrology - applications of TESCAN integrated mineral analyzer (TIMA). J. Geosci. 63, 47–63. https://doi.org/10.3190/jgeosci.250.
Hu, C.L., Li, Z.J., 2015. A review on the mechanical properties of cement-based materials measured by nanoindentation. Constr. Build. Mater. 90, 80–90. https://doi.org/10.1016/j.conbuildmat.2015.05.008.
Hu, S.Y., Bai, B., Tao, S.Z., et al., 2022. Heterogeneous geological conditions and differential enrichment of medium and high maturity continental shale oil in China. Petrol. Explor. Dev. 49 (2), 257–271. https://doi.org/10.1016/S1876-3804(22)60022-3.
Hu, T., Pang, X.Q., Jiang, F.J., 2024. Whole petroleum system theory and new directions for petroleum geology development. Adv. Geo-Energy Res. 11, 1–5. https://doi.org/10.46690/ager.2024.01.01.
Huang, Y.X., Shi, Z., Li, J., Zhang, T.C., Chen, Z.W., 2025. Quantifying the mechanical properties of coal matrix and cleat using digital image correlation method. Deep Resour. Eng. 2, 100168. https://doi.org/10.1016/j.deepre.2025.100168.
Hupp, B.N., Donovan, J.J., 2018. Quantitative mineralogy for facies definition in the Marcellus Shale (Appalachian Basin, USA) using XRD-XRF integration. Sediment. Geol. 371, 16–31. https://doi.org/10.1016/j.sedgeo.2018.04.007.
Johnston, J.E., Christensen, N.I., 1995. Seismic anisotropy of shales. J. Geophys. Res. Solid Earth 100, 5991–6003. https://doi.org/10.1029/95JB00031.
Kahle, M., Kleber, M., Jahn, R., 2002. Review of XRD-based quantitative analyses of clay minerals in soils: The suitability of mineral intensity factors. Geoderma 109, 191–205. https://doi.org/10.1016/S0016-7061(02)00175-1.
Kumar, V., Sondergeld, C.H., Rai, C.S., 2012. Nano to macro mechanical characterization of shale. In: Presented at the SPE Annual Technical Conference and Exhibition. OnePetro. https://doi.org/10.2118/159804-MS.
Li, L.H., Huang, B.X., Tan, Y.F., Deng, X.L., Li, Y.Y., Zheng, H., 2017. Geometric heterogeneity of continental shale in the Yanchang Formation, southern Ordos Basin, China. Sci. Rep. 7, 6006. https://doi.org/10.1038/s41598-017-05144-z.
Li, Y., Wang, Z.S., Pan, Z.J., Niu, X.L., Yu, Y., Meng, S.Z., 2019. Pore structure and its fractal dimensions of transitional shale: A cross-section from east margin of the Ordos Basin, China. Fuel 241, 417–431. https://doi.org/10.1016/j.fuel.2018.12.066.
Li, S.X., Niu, X.B., Liu, G.D., Li, J.H., Sun, M.L., You, F.L., He, H.N., 2020. Formation and accumulation mechanism of shale oil in the 7th Member of Yanchang Formation, Ordos Basin. Oil Gas Geol. 41, 719–729.
Li, L.H., Huang, B.X., Tan, Y.F., Li, X., Ranjith, P.G., 2022. Using micro-indentation to determine the elastic modulus of shale laminae and its implication: Cross-scale correlation of elastic modulus of mineral and rock. Mar. Pet. Geol. 143, 105740. https://doi.org/10.1016/j.marpetgeo.2022.105740.
Li, M., Guo, P.J., Stolle, D., Liu, S.Y., 2023. Modeling method for rock heterogeneities and multiple hydraulic fractures propagation based on homogenization approach and PHF-LSM. Geomech. Energy Environ. 33, 100442. https://doi.org/10.1016/j.gete.2023.100442.
Liang, C., Cao, Y.C., Liu, K.Y., Jiang, Z.X., Wu, J., Hao, F., 2018. Diagenetic variation at the lamina scale in lacustrine organic-rich shales: Implications for hydrocarbon migration and accumulation. Geochem. Cosmochim. Acta 229, 112–128. https://doi.org/10.1016/j.gca.2018.03.017.
Liao, Q.Z., Wang, B., Chen, X., Tan, P., 2024. Reservoir stimulation for unconventional oil and gas resources: Recent advances and future perspectives. Adv. Geo-Energy Res. 13, 7–9.
Lichinchi, M., Lenardi, C., Haupt, J., Vitali, R., 1998. Simulation of Berkovich nanoindentation experiments on thin films using finite element method. Thin Solid Films 312, 240–248. https://doi.org/10.1016/S0040-6090(97)00739-6.
Lin, C., He, J.M., Li, X., Wan, X.L., Zheng, B., 2017. An experimental investigation into the effects of the anisotropy of shale on hydraulic fracture propagation. Rock Mech. Rock Eng. 50, 543–554. https://doi.org/10.1007/s00603-016-1136-4.
Liu, K.Q., Ostadhassan, M., Bubach, B., 2016. Applications of nano-indentation methods to estimate nanoscale mechanical properties of shale reservoir rocks. J. Nat. Gas Sci. Eng. 35, 1310–1319. https://doi.org/10.1016/j.jngse.2016.09.068.
Liu, Y.W., Liu, A., Liu, S.M., Kang, Y., 2022. Nano-scale mechanical properties of constituent minerals in shales investigated by combined nanoindentation statistical analyses and SEM-EDS-XRD techniques. Int. J. Rock Mech. Min. Sci. 159, 105187. https://doi.org/10.1016/j.ijrmms.2022.105187.
Liu, K.Q., Hosseinzadeh, S., Safaei-Farouji, M., Liu, B., Morta, H.B., Ostadhassan, M., 2023. Fracture toughness of organic rich shale via nanoindentation: A comparison of energy-based methods. Geoenergy Sci. Eng. 225, 211695.
Lo, T., Coyner, K.B., Toksöz, M.N., 1986. Experimental determination of elastic anisotropy of Berea sandstone, Chicopee shale, and Chelmsford granite. Geophysics 51, 164–171. https://doi.org/10.1190/1.1442029.
Loucks, R.G., Reed, R.M., Ruppel, S.C., Jarvie, D.M., 2009. Morphology, genesis, and distribution of nanometer-scale pores in siliceous mudstones of the mississippian barnett shale. J. Sediment. Res. 79, 848–861. https://doi.org/10.2110/jsr.2009.092.
Lyu, Q.Q., Fu, J.H., Luo, S.S., Li, S.X., Zhou, X.P., Pu, Y.X., Yan, H.G., 2022. Sedimentary characteristics and model of gravity flow channel-lobe complex in a depression lake basin: A case study of Chang 7 Member of Triassic Yanchang Formation in southwestern Ordos Basin, NW China. Petrol. Explor. Dev. 49, 1323–1338. https://doi.org/10.1016/S1876-3804(23)60352-0.
Madenova, Y., Madani, N., 2021. Application of Gaussian mixture model and geostatistical Co-simulation for resource modeling of geometallurgical variables. Nat. Resour. Res. 30, 1199–1228. https://doi.org/10.1007/s11053-020-09802-4.
Manjunath, G.L., Jha, B., 2019. Geomechanical characterization of gondwana shale across nano-micro-meso scales. Int. J. Rock Mech. Min. Sci. 119, 35–45. https://doi.org/10.1016/j.ijrmms.2019.04.003.
Mavko, G., Mukerji, T., Dvorkin, J., 2020. The rock physics handbook. Cambridge university press.
Meng, S.W., Li, D.X., Liu, X., Zhang, Z.H., Tao, J.P., Yang, L., Rui, Z.H., 2023a. Study on dynamic fracture growth mechanism of continental shale under compression failure. Gas Sci. Eng. 114, 204983. https://doi.org/10.1016/j.jgsce.2023.204983.
Meng, S.W., Zhang, Z.H., Tao, J.P., Zhang, C.Q., Yang, L., Xu, J.C., 2023b. A novel upscaling method for evaluating mechanical properties of the shale oil reservoir based on cluster analysis and nanoindentation. J. Energy Resour. Technol. 145, 112901. https://doi.org/10.1115/1.4062248.
Mori, T., Tanaka, K., 1973. Average stress in matrix and average elastic energy of materials with misfitting inclusions. Acta Metall. 21, 571–574.
Oliver, W.C., Pharr, G.M., 1992. An improved technique for determining hardness and elastic modulus using load and displacement sensing indentation experiments. J. Mater. Res. 7, 1564–1583.
Richardson, W.H., 1972. Bayesian-based iterative method of image restoration. JoSA 62, 55–59.
Sami Ullah Khan, Wasim Jamshed, 2023. Finite Element Analysis and Wear Rate Analysis of Nano Coated High Speed Steel Tools for Industrial Application. Babylon. J. Mech. Eng. 2023, 13–19. https://doi.org/10.58496/BJME/2023/002.
Schuh, C.A., 2006. Nanoindentation studies of materials. Mater. Today 9, 32–40.
Shukla, P., Kumar, V., Curtis, M., Sondergeld, C.H., Rai, C.S., 2013. Nanoindentation studies on shales. In: Presented at the 47th U.S. Rock Mechanics/Geomechanics Symposium. ARMA-2013-578.
Sone, H., Zoback, M.D., 2013. Mechanical properties of shale-gas reservoir rocks — Part 1: Static and dynamic elastic properties and anisotropy. Geophysics 78, D381–D392. https://doi.org/10.1190/geo2013-0050.1.
Sun, Z.H., Elsworth, D., Cui, G.L., Li, Y.C., Zhu, A.Y., Chen, T.Y., 2024. Impacts of rate of change in effective stress and inertial effects on fault slip behavior: New insights into injection-induced earthquakes. J. Geophys. Res. Solid Earth 129, e2023JB027126. https://doi.org/10.1029/2023JB027126.
Szabó, N.P., Braun, B.A., Abdelrahman, M.M.G., Dobróka, M., 2021. Improved well logs clustering algorithm for shale gas identification and formation evaluation. Acta Geod. Geophys. 56, 711–729. https://doi.org/10.1007/s40328-021-00358-0.
Tan, J.Q., Horsfield, B., Fink, R., Krooss, B., Schulz, H.-M., Rybacki, E., Zhang, J., Boreham, C.J., van Graas, G., Tocher, B.A., 2014. Shale gas potential of the major marine shale formations in the upper Yangtze platform, South China, Part III: Mineralogical, Lithofacial, Petrophysical, and rock mechanical properties. Energy Fuels 28, 2322–2342. https://doi.org/10.1021/ef4022703.
Tricarico, M., Tan, J.C., 2022. Mechanical properties and nanostructure of monolithic zeolitic imidazolate frameworks: A nanoindentation, nanospectroscopy, and finite element study. Mater. Today Nano 17, 100166. https://doi.org/10.1016/j.mtnano.2021.100166.
Ulm, F.J., Abousleiman, Y., 2006. The nanogranular nature of shale. Acta Geotech 1, 77–88.
Vernik, L., Milovac, J., 2011. Rock physics of organic shales. Lead. Edge 30, 318–323. https://doi.org/10.1190/1.3567263.
Wang, Z.J., Wang, H., Cates, M.E., 2001. Effective elastic properties of solid clays. Geophysics 66, 428–440.
Wang, X.Z., Gao, S.L., Gao, C., 2014. Geological features of Mesozoic lacustrine shale gas in south of Ordos Basin, NW China. Petrol. Explor. Dev. 41, 326–337. https://doi.org/10.1016/S1876-3804(14)60037-9.
Wang, R.R., Zhou, J., Jiang, H., Han, S.Y., Wang, L., Wang, D., Chen, Y.H., 2021. A general transfer learning-based Gaussian mixture model for clustering. Int. J. Fuzzy Syst. 23, 776–793. https://doi.org/10.1007/s40815-020-01016-3.
Wang, J.F., Yang, C., Liu, Y.K., Xiong, Y.Q., 2022. Nanoindentation investigation of mechanical and creep properties of continental Triassic Yanchang Formation shale, Ordos Basin. Interpretation 10, SJ29–SJ41. https://doi.org/10.1190/INT-2021-0218.1.
Wu, Y.K., Li, Y.C., Luo, S.M., Lu, M., Zhou, N., Wang, D.F., Zhang, G.P., 2020. Multiscale elastic anisotropy of a shale characterized by cross-scale big data nanoindentation. Int. J. Rock Mech. Min. Sci. 134, 104458. https://doi.org/10.1016/j.ijrmms.2020.104458.
Yan, Q., Zhang, W.Z., Peng, P.G., Zhou, Z.J., 2009. Occurrence and concentration of uranium in the hydrocarbon source rocks of Chang 7 Member of Yanchang Formation, Ordos Basin. Acta petrol. Sin. 25, 2469–2476.
Yang, C., Xiong, Y.Q., Wang, J.F., Li, Y., Jiang, W.M., 2020. Mechanical characterization of shale matrix minerals using phase-positioned nanoindentation and nano-dynamic mechanical analysis. Int. J. Coal Geol. 229, 103571. https://doi.org/10.1016/j.coal.2020.103571.
Yuan, X.J., Lin, S.H., Liu, Q., Yao, J.L., Wang, L., Guo, H., Deng, X., Cheng, D., 2015. Lacustrine fine-grained sedimentary features and organicrich shale distribution pattern: A case study of Chang 7 Member of Triassic Yanchang Formation in Ordos Basin, NW China. Petrol. Explor. Dev. 42, 37–47. https://doi.org/10.1016/S1876-3804(15)60004-0.
Zargari, S., Prasad, M., Mba, K.C., Mattson, E.D., 2011. Organic maturity, hydrous pyrolysis and elastic property in shales. In: Canadian Unconventional

Resources Conference. SPE, Calgary, Alberta, Canada. https://doi.org/10.2118/149403-MS.

Zhang, T.S., Hu, S.Y., Bu, Q.Y., Bai, B., Tao, S.Z., Chen, Y., Pan, Z., Lin, S., Pang, Z., Xu, W., Yuan, M., Fan, J., Sun, Y., Feng, X., 2021. Effects of lacustrine depositional sequences on organic matter enrichment in the Chang 7 Shale, Ordos Basin, China. Mar. Pet. Geol. 124, 104778. https://doi.org/10.1016/j.marpetgeo.2020.104778.

Zhang, X.J., He, J.H., Deng, H.C., Fu, M.Y., Xiang, Z.H., Peng, X., Gluyas, J.G., Li, R., 2022. Controls of interlayers on the development and distribution of natural fractures in lacustrine shale reservoirs: A case study of the Da'anzhai member in the Fuling area in the eastern Sichuan Basin. J. Pet. Sci. Eng. 208, 109224. https://doi.org/10.1016/j.petrol.2021.109224.

Zhang, Q., Zou, J.P., Jiao, Y.Y., Gao, J.P., 2025. Practice and validation of inversion of seismic source localisation based on genetic algorithm. Deep Resour. Eng. 2, 100164. https://doi.org/10.1016/j.deepre.2024.100164.

Zhao, K., Du, X.B., Lu, Y.C., Xiong, S.P., Wang, Y., 2019. Are light-dark coupled laminae in lacustrine shale seasonally controlled? A case study using astronomical tuning from 42.2 to 45.4 Ma in the Dongying Depression, Bohai Bay Basin, Eastern China. Palaeogeogr. Palaeoclimatol. Palaeoecol. 528, 35–49. https://doi.org/10.1016/j.palaeo.2019.04.034.

Zhu, S.N., Yin, Y.P., Li, B., Wei, Y.J., 2019. Shear creep characteristics of weak carbonaceous shale in thick layered Permian limestone, Southwestern China. J. Earth Syst. Sci. 128, 28. https://doi.org/10.1007/s12040-018-1051-z.